Study of Lepton Selection Cut Efficiency for $WH \to WWW$ Analysis

The Graduate School of
Department of Mathematics Faculty of Science
(*Master Course*)
Osaka City University
High Energy Physics Lab.

Takayuki Wakisaka

March 1, 2006

Abstract

We estimate lepton selection cut efficiency and scale factor using $Z \to \ell\ell$. This analysis is for Higgs search in the following mode:

$$qq' \to W^{\pm}H \to W^{\pm}W^{*}W^{*} \to \ell^{\pm}\nu\ell^{\pm}\nu + X.$$

In the Standard Model, the Higgs boson has coupling strength proportional to the mass of the particle, and in fact is responsible for the mass of the particle. But, no experiment has directly detected the existence of the Higgs boson. Now, we would like to serach Higgs boson in particular "Bosophilic Higgs boson" using above mode. The our Higgs mode has like-sign dilepton in the final state, so it suppress QCD background. In hadron collisions, this mode is cleanest signature.

We have to estimate lepton selection cut efficiency and scale factor due to serach the Higgs boson in the our Higgs boson mode. The lepton selection is done by appling geometrical, kinematical, isolation and identification cuts. The selection cut efficiency is written in the following

$$\varepsilon_{\mathrm{tot}} = A \cdot \varepsilon_{\mathrm{Iso}} \cdot \varepsilon_{\mathrm{ID}} \cdot \varepsilon_{\mathrm{rec}} \cdot \varepsilon_{\mathrm{trig}}.$$

The scale factor is (Data efficiency)/(efficiency MC), the MC $Z \to \ell\ell$ ($\ell = e$, μ) samples are generated by PYTHIA. We now use basically standard lepton selection criteria in the CDF analysis. The CDF is the proton-antiproton collision experiment at the Tevatron, which is the accelerator in $\sqrt{s} = 1.96$ TeV. What we should emphasize is that we require kinematical cut of greater than 6 GeV/c^2 to the 2nd leg lepton, while for the 1st leg one, that of greater than 20 GeV/c^2, The reason of 6 GeV cuts is that the lepton dacaying from off-shell W^* has low energy.

We also estimate $\gamma^*/Z^0 \to \ell\ell$ cross sections due to validate this selection cut for lepton selection in the CDF Run II data coresponding to an integrated luminosity of 29.4 pb^{-1} for $\gamma^*/Z^0 \to ee$ and that of 52.4 pb^{-1} for $\gamma^*/Z^0 \to \mu\mu$ each. The Z leptonic decay is well established. We get the following results:

$$\sigma_{\gamma^*/Z^0 \to ee} = 232.1 \pm 8.1 \text{ pb}$$
$$\sigma_{\gamma^*/Z^0 \to \mu\mu} = 240.1 \pm 8.1 \text{ pb}.$$

Therefore more, we compare this cross section with CDF Run II official results. From the comparisons, we get the difference of 9.2 % for $\gamma^*/Z^0 \to ee$ cross section, and the difference of 3.2 % for $\gamma^*/Z^0 \to \mu\mu$. So, this mehods of lepton selection cuts is validated for lepton selection.

Acknowledgments

I would like to thank Prof. Toru Okusawa. He gave me interested physical study, and taught basically most important physics. I would like to thank Prof. Yoshihiro Seiya. He led me precise analytical technique and taught about "What is a theoretical thought?". I would like to thank Dr. Kazuhiro Yamamoto for his guidence and technical supports, moreover I felt admiration at his accurate work. I would like to thank Dr. Hirokazu Kobayashi. He taught me the base of the program and analysis though his work was busy. I would like to thank grduated students, Toshiyuki Sakai and Junichi Hiramoto. They thought about several problems with me. I would like to student member of Osaka City University, Daiki Yanagida, Masashi Nishikawa and Keishuke Maeda. I am glad to spend the same time with them. I want to express my gratitude to a lot of other people who supported me.

Finally, I would like to thank my family for your support of my life and an economic.

Contents

1 Introduction **1**
1.1 The Standard Model . . . 1
1.1.1 Fermion and Boson . . . 1
1.1.2 Quantum Electordynamics (QED) . . . 2
1.1.3 Quantum Chromodynamics (QCD) . . . 4
1.1.4 Electroweak Theory and The Higgs Mechanism . . . 5
1.2 The Sandard Model Higgs Boson Search . . . 8
1.3 The Bosophilic Higgs Boson . . . 10
1.4 Physics Motivation and Previous Result . . . 11

2 The Experiment Apparatus **13**
2.1 The Tevatron . . . 13
2.1.1 Proton Beam . . . 13
2.1.2 Antiproton Beam . . . 14
2.2 The Collider Detector at Fermilab . . . 14
2.2.1 The CDF Coordinate System . . . 15
2.2.2 Charged Particle Tracking Systems . . . 17
2.2.3 Calorimeters . . . 20
2.2.4 Muon Chambers . . . 23
2.2.5 Luminosity Monitors . . . 24
2.3 Trigger Systems . . . 25
2.3.1 Level-1 . . . 25
2.3.2 Level-2 . . . 26
2.3.3 Level-3 . . . 26

3 Lepton Selection Cut Efficiency and Scale Factor **28**
3.1 Lepton Selection Variables . . . 28
3.1.1 Event Selection Variable . . . 28
3.1.2 Electron Selection Variables . . . 28
3.1.3 Muon Selection Variables . . . 33
3.2 Selection Cut Efficiency . . . 39
3.2.1 Geometrical and Kinematical Acceptance . . . 39
3.2.2 Isolation Cut Efficiency . . . 40
3.2.3 Identification Cut Efficiency . . . 43
3.3 Reconstruction Efficiency and Sacle Factor for Muon chamber . . . 50
3.4 Trigger Efficiency . . . 50

4 $\gamma^*/Z^0 \to \ell\ell$ Cross Section **54**
4.1 Total Efficiency 54
4.2 Cross Section and Comparing to CDF Run II Result 55

5 Conclusions **57**

List of Figures

1.1 The higgs potential V for a cpmplex scalar field with $\nu^2 < 0$ and $\lambda > 0$. . . 7
1.2 Standard Model Higgs boson interactions at tree-level. 9
1.3 Branching ratios of the dominant decay modes of the Standard Model Higgs boson. 9
1.4 Higgs boson production cross section at the Tevatron for the various production mechnisms. 10
1.5 Branching ratio of a bosophilic Higgs boson decay. 10
1.6 Previous cross section upper limit at 95 % confidence level as a function of Higgs boson mass. 12
1.7 CDF Run II preliminary cross section limit for the Standard Model Higgs boson. 12

2.1 The Tevatron Accelerator chain. 14
2.2 Cut away view of the CDF Run II detector. 15
2.3 Elevation view of one half of the CDF II detector. 16
2.4 Longitudinal view of the CDF tracking system, represnting quarter of the detector. 17
2.5 $r - \phi$ view of the silicon detectors. 19
2.6 A view of the three barrels of the SVX sillicon detector. 19
2.7 1/6 section of the COT end plate. For each superlayer is given the total number of supercells, the wire orientation (axial or stereo), and the average radius. 21
2.8 The cross section of upper part of the end plug calorimeter. 23
2.9 Muon detector coverage. 25
2.10 Block diagram of the CDF II trigger system. 27

3.1 The electron variables used for the selection of events. The loose electron in the $Z \to e^+e^-$ candidates events. All the selection cut are applied each variable excluding the variable itself (Isolation, HAD/EM, $L_{\rm shr}$, E/p and $\chi^2_{\rm strip}$). 31
3.2 The electron variables used for the selection of events. The loose electron in the $Z \to e^+e^-$ candidates events. All the selection cut are applied each variable excluding the variable itself ($\Delta z_{\rm CES}$, $Q \times \Delta x_{\rm CES}$, $z_0 - z_{\rm vtx}$ and d_0). 32
3.3 The muon variables used for the selection of events. The loose muon in the $Z \to \mu^+\mu^-$ candidates events. All the selection cut are applied each variable excluding the variable itself (Isolation, EM). 35
3.4 The muon variables used for the selection of events. The loose muon in the $Z \to \mu^+\mu^-$ candidates events. All the selection cut are applied each variable excluding the variable itself (HAD and $r \times \Delta\phi$). 36

3.5 The muon variables used for the selection of events. The loose muon in the $Z \to \mu^+\mu^-$ candidates events. All the selection cut are applied each variable excluding the variable itself ($z_0 - z_{\mathrm{vtx}}$ and d_0). 37
3.6 The matched lepton dR distributions (left: electron, right: muon). The red lines are dR cut values. 40
3.7 Isolation cut efficiency. From upper to lower: This analysis, Previous analysis and Scale Factor and Data ratio. 42
3.8 Electron identification cut efficiency. From upper to lower: This analysis, Previous analysis and Scale Factor and Data ratio. 45
3.9 Muon identification cut efficiency (CMUP-CMUP). From upper to lower: This analysis, Previous analysis and Scale Factor and Data ratio. 46
3.10 Muon identification cut efficiency (CMX-CMUP). From upper to lower: This analysis, Previous analysis and Scale Factor and Data ratio. 47
3.11 Muon identification cut efficiency (CMX-CMX). From upper to lower: This analysis, Previous analysis and Scale Factor and Data ratio. 48
3.12 Muon identification cut efficiency (CMUP-CMX). From upper to lower: This analysis, Previous analysis and Scale Factor and Data ratio. 49
3.13 The η distribution (left figure) and Reconstrction efficiency each 0.1 η (right one). for the 1st muon CMUP. The upper two figures are from Data sample, the lower two figures are MC. 51
3.14 The η distribution (left figure) and Reconstrction efficiency each 0.1 η (right one). for the 1st muon CMX. The upper two figures are from Data sample, the lower two figures are MC. 52

4.1 γ^*/Z^0 mass distributions in HEPG level. The left figure is $\gamma^*/Z^0 \to ee$, the right one is $\gamma^*/Z^0 \to \mu\mu$. The red line is the fitting function. 55
4.2 $\gamma^*/Z^0 \to \ell\ell$ Cross section for this anlysis and CDF Run II official result. 56

List of Tables

1.1 The properties of the leptons. The electric charge are given in units of proton charge and the spins are given in units of $\hbar$. 2
1.2 The properties of the quarks. The electric charge are given in units of proton charge and the spins are given in units of $\hbar$. 2
1.3 Interaction and Guage boson 2

2.1 Design parameters of SVX detector at CDF. 18
2.2 Design parameters of COT detector at CDF. 20
2.3 Design parameters of the calorimeter at CDF. 23
2.4 Design parameters of the muon detectors at CDF. Pion interaction lengths and multiple scattering are computed at s reference angle of $\theta = 90°$ in CMU and CMP/CSP, at an angle of 55° in CMX/CSX, and show the range of values for the BMU. 24

3.1 Primary vertex and lepton selection cuts 38
3.2 The geomatriacal and kinematical Acceptance with $p_T > 6$ GeV/c lepton on the HEPG and CDF level. 40
3.3 The ratio of remaning events after the geometrical to kinematical cut. The Ratio = CDF/HEPG. 40
3.4 Isolation cut efficiency for $Z \rightarrow \ell\ell$ Data and MC, also show previous result. 41
3.5 The difference in the efficiency on account of cut methods and offline release versions using MC. 41
3.6 Electron identification cut efficiency for $Z \rightarrow ee$ Data and MC. 43
3.7 Muon identification cut efficiency for $Z \rightarrow \mu\mu$ Data and MC. From upper to lower: CMUP-CMUP, CMX-CMUP, CMX-CMX, CMUP-CMX. . . . 44
3.8 Reconstution efficiency and Scale Factor. 50
3.9 Trigger efficiency which is refferred to [14] and [15] 50

4.1 The number of Observed γ^*/Z^0 events and the Total efficiency for Data and MC. 55
4.2 $\gamma^*/Z^0 \rightarrow \ell\ell$ Cross Section (pb) for this analysis and CDF Run II Result (left table, The error is only statistic error). The right side table shows cross section breacking down muon types (CMUP-CMUP, CMX-CMUP, CMX-CMX and CMUP-CMX). 56

Chapter 1

Introduction

Elementary particle physics deals with the study of the elementary constituent of matter and their interaction. The elementary particles are the most basic physical constituents of the universe. The behavior of all known the elementary particles can be described within so called the Standard Model. The Standard Model is the most successful thory of elementary particles and thier interactions. This model incorporates the quarks and leptons as well as their interactions through the strong, weak and electromagnetic forces. Only gravity remains outside the Standard Model. The force-carrying particles are called gauge bosons, and they differ fundamentally from the quarks and leptons called ferimon. The fundamental forces appear to behave very differently in ordinary matter, but the Standard Model indicates that they are basically very similar when matter is in a high-energy environment. This chapter will briefly describe the Standard Model of Particle Physics.

1.1 The Standard Model

The elementary pariticles of Satandard Model can be classified into two types; particles with half-integral spin are called fermions because they obey Fermi-Dirac statistics, while those with integral spin obey Bose-Einstein statistics and are called bosons.

1.1.1 Fermion and Boson

The fermions can be classified into six leptons and six quarks according to integral electric charge and fractional one.

The leptons are integral electric charge. The three charged leptons are electron, muon and tau. They differ in the values of their masses. The other three leptons, the neutrions (ν), are electrically neutral and have very small mass. Every particles has an antiparticles. A particle and its associated antiparticle have the same mass, spin and liftime. Their electric charge is the same in magnitude but differs sign. Table 1.1 is shown in the properties of the leptons.

The quarks are fractional electric charge. The six quarks are called up (u), down (d), charm (c), strange (s), top (t) and bottom (b). The u, c, t quarks are a chrage of 2/3, while The d, s, b quarks are of $-1/3$. Table is shown in the properties of the quarks.

There are four known forces which act on matter. Three have a basis with the SM, electromagnetic, weak and strong. The gravatational force is negligibly small at the energy scales at which the SM is thought to be relevant, and it is not included. The electromagnetic, weak and strong froces are mediated by the spin-1 gauge bosons.

Although the gravitational interaction is not featured in the SM, it is thought to be mediated by a spin-2 gauge boson, known as the gravition.

Lepton	Mass	Charge	Spin
ν_e	< 3 eV/c^2	0	1/2
e^-	0.511 MeV/c^2	-1	1/2
ν_μ	< 0.19 MeV/c^2	0	1/2
μ^-	105.66 MeV/c^2	-1	1/2
ν_τ	< 18.2 MeV/c^2	0	1/2
τ^-	1.777 GeV/c^2	-1	1/2

Table 1.1: The properties of the leptons. The electric charge are given in units of proton charge and the spins are given in units of $\hbar$.

Quark	Mass	Charge	Spin
u	1.5 - 4.0 MeV/c^2	2/3	1/2
d	4 - 8 MeV/c^2	$-1/3$	1/2
c	1.15 - 1.35 MeV/c^2	2/3	1/2
s	80 - 130 MeV/c^2	$-1/3$	1/2
t	172.7 $\pm$ 2.9 GeV/c^2	2/3	1/2
b	4.1 - 4.4 GeV/c^2	$-1/3$	1/2

Table 1.2: The properties of the quarks. The electric charge are given in units of proton charge and the spins are given in units of $\hbar$.

Interaction	Effective coupling	Boson	Mass[GeV/c^2]	Range[cm]	Typical time[s]
Gravitation	10^{-39}	gravition	0	∞	-
Electromagnetism	1/137	photon	0	∞	10^{-20}
Weak	10^{-5}	$W^\pm$, Z^0	80.4, 91.2	10^{-16}	10^{-10}
Strong	$\sim$1	gluon	0	10^{-13}	10^{-23}

Table 1.3: Interaction and Guage boson

1.1.2 Quantum Electordynamics (QED)

QED has the structure of an Abelian gauge theory with a $U(1)$ gauge group. The gauge field which mediates the interaction between the charged spin-1/2 fields is the electromagnetic field. For example, an electron is described by a complex field and the Lagrangian is

$$\mathscr{L} = i\bar{\psi}\gamma_\mu\partial^\mu\psi - m\psi\bar{\psi}. \tag{1.1}$$

The Lagrangian is invariant under the phase tramsformation

$$\psi \to e^{i\alpha}\psi \tag{1.2}$$

where α is a real constant. The family phase transformations $U(\alpha) \equiv e^{i\alpha}$ forms a unitary Abelian group known as the $U(1)$ group. Throgh Nether's theorem, this invarant implies the extence of a conserved current and charge

$$\partial_\mu j^\mu = 0, \qquad j^\mu = -e\bar{\psi}\gamma^\mu\psi, \qquad Q = \int d^3x j^0. \tag{1.3}$$

But, we should generalize (1.2) to the transformation

$$\psi \to e^{i\alpha(x)}\psi, \tag{1.4}$$

where $\alpha(x)$ now depends on space and time in a completely arbitrary way. This is known as local gauge invariance. However, this is not work. The Lagrangian (1.1) is not invariant under such phase transformation. From (1.4),

$$\bar{\psi} \to e^{-i\alpha(x)}\bar{\psi}, \tag{1.5}$$

so the last term of Lagrangian is invariant; however, the derivative of ψ does not follow (1.4). Rather,

$$\partial_\mu \to e^{i\alpha(x)}\partial_\mu\psi + ie^{i\alpha(x)}\psi\partial_\mu\alpha, \tag{1.6}$$

and the $\partial_\mu\alpha$ term breaks the invariant of Lagrangian. To impose invariance of the Lagrangian under local guage transformation, we must seek a modified derivative, D_μ, that transforms covariantly under phase transformation,

$$D_\mu\psi \to e^{i\alpha(x)}D_\mu\psi. \tag{1.7}$$

To form the covariant derivative D_μ, we must intordcuce a vector field A_μ with transformation properties such that the unwanted term in (1.6) is canceled. This can be accomplished by the construction

$$D_\mu\psi \equiv \partial_\mu - ieA_\mu, \tag{1.8}$$

where A_μ transfroms as

$$A_\mu \to A_\mu + \frac{1}{e}\partial_\mu\alpha. \tag{1.9}$$

Invariance of the Lagrangian (1.1) is acheived by replacing ∂_μ by D_μ:

$$\begin{aligned}\mathscr{L} &= i\bar{\psi}\gamma_\mu D^\mu\psi - m\psi\bar{\psi} \\ &= \bar{\psi}(i\gamma^\mu\partial_\mu - m)\psi + e\bar{\psi}\gamma^\mu\psi A_\mu.\end{aligned} \tag{1.10}$$

Hence, by demanding local phase invariance, we are forced to indroduce a vector fieldA_μ, called gauge field. if we are to regard this new field as the physical photon field, we must add to the Lagrangian a term corresponding to its kinetic. Since the kinetic term must be invariant under (1.9), it can only involve the gauge invariant field strength tentor

$$F_{\mu\nu} = \partial_\mu A_\nu - \partial_\nu A_\mu. \tag{1.11}$$

We are thus led to the Lagrangian of QED.

$$\mathscr{L} = \bar{\psi}(i\gamma^\mu\partial_\mu - m)\psi + e\bar{\psi}\gamma^\mu\psi A_\mu - \frac{1}{4}F_{\mu\nu}F^{\mu\nu} \tag{1.12}$$

The addition of a mass term $(1/2)m^2A_\mu A^\mu$ is prohibited by gauge invariance. The gauge particle must be massless and expect the gauge field to the infinite range.

1.1.3 Quantum Chromodynamics (QCD)

Quantum Chromodynamics (QCD) is the gauge theory for strong interactions. QCD is based on the extension of the QED idea, but with the $U(1)$ gauge group repalced by the $SU(3)$ group of phase transformations on the quark color fields. The Lagrangian is

$$\mathscr{L} = \bar{q}_j(i\gamma^\mu \partial_\mu - m)q_j \tag{1.13}$$

where q_1, q_2, q_3 denote the three color fields. We require Lagrangian to be invariant under local phase transformations of the form

$$q(x) \to Uq(x) \equiv e^{i\alpha_a(x)T_a} q(x), \tag{1.14}$$

where U is an arbitary 3×3 unitary matrix. A summation over the repeated suffix a is implied. $T_a(a = 1, \cdots, 8)$ are a set of linearly independent traceless 3×3 matricies, and α_a are the group parameters. The group is non-Abelian since the gernerators T_a do not commute with each other.

$$[T_a, T_b] = if_{abc}T_c \tag{1.15}$$

where f_{abc} are real constants, called the structure constants of the group. To impose $SU(3)$ local gauge invariance on the Lagrangian (1.13), consider inifinitesmal phase transformations

$$q(x) \to [1 + i\alpha_a(x)T_a]q(x) \tag{1.16}$$
$$\partial_\mu q \to (1 + i\alpha_a T_a)\partial_\mu q + iT_a q \partial_\mu \alpha_a. \tag{1.17}$$

The last term spoils the invariance of Lagrangian. So, to impose invariance of the Lagrangian under local guage transformation, we intorduce 8 gauge fields G^a_μ, each transforming as

$$G^a_\mu \to G^a_\mu - \frac{1}{g}\partial_\mu \alpha_a - f_{abc}\alpha_b G^c_\mu, \tag{1.18}$$

and form a covariant derivative

$$D_\mu = \partial_\mu + igT_a D^a_\mu. \tag{1.19}$$

We then make the replacement $\partial_\mu \to D_\mu$ in the Lagrangian (1.13), and add a gauge invariant kinetic energy term for each of the G^a_μ fields. The final gauge invariant QCD Lagrangian is

$$\mathscr{L} = \bar{q}(i\gamma^\mu \partial_\mu - m)q - g(\bar{q}\gamma^\mu T_a q)G^a_\mu - \frac{1}{4}G^a_{\mu\nu}G^{\mu\nu}_a \tag{1.20}$$
$$G^a_{\mu\nu} = \partial_\mu G^a_\nu - \partial_\nu G^a_\mu - gf_{abc}G^b_\mu G^c_\nu \tag{1.21}$$

(1.20) is the Lagrangian for interacting colored quarks q and vector gluons G_μ, with coupling specified by g. Local gauge invariance requires the gluons to be massless. The field strength $G^a_{\mu\nu}$ has a remakable new property on accont of the extra term in (1.21). Imposing the gauge symmetry has required that the kinetic energy term in Lagrangian is not purely kinetic but includes an induced self-interaction between the gauge bosons and reflect the fact that gluons themselves carry color charge. We emphasize that gauge invariance uniqely determines the structure of these gluon self-coupling terms.

1.1.4 Electroweak Theory and The Higgs Mechanism

Electroweak Theory presents a unified description of electromagnetism and the weak interaction, which is based upon the symmetry group $SU(2)_L \otimes U(1)_Y$. We are led to the electroweak Lagrangian by requiring an $SU(2)_L \otimes U(1)_Y$ invariant form. For example, for the electron-neutrino lepton pair, we have

$$\begin{aligned} \mathscr{L}_1 = \chi_L \gamma^\mu \left[i\partial_\mu - \frac{2}{g}\boldsymbol{\tau}\cdot\boldsymbol{W}_\mu + \frac{g'}{2}B_\mu \right] \chi_L, \\ + \bar{\psi}_R \gamma^\mu \left[i\partial_\mu + g' B_\mu \right] \psi_R - \frac{1}{4}\boldsymbol{W}_{\mu\nu}\cdot\boldsymbol{W}^{\mu\nu} - \frac{1}{4}B_{\mu\nu}B^{\mu\nu} \end{aligned} \tag{1.22}$$

where the left-handed fermions form isospin doublet χ_L and the right-handed fermions are isosinglets ψ_R

$$\chi_L = \begin{pmatrix} \nu \\ e^- \end{pmatrix}_L, \qquad \psi_R = e^-{}_R, \tag{1.23}$$

and $\boldsymbol{W}^\mu$, B^μ are vector bosons.

$$\boldsymbol{W}_{\mu\nu} = \partial_\mu \boldsymbol{W}_\nu - \partial_\nu \boldsymbol{W}_\mu - g\boldsymbol{W}_\mu \times \boldsymbol{W}_\nu, \tag{1.24}$$

$$B_{\mu\nu} = \partial_\mu B_\nu - \partial_\nu B_\mu. \tag{1.25}$$

We must impose local gauge invariance,

$$\chi_L = \chi'_L = e^{i\boldsymbol{\alpha}(\boldsymbol{x})\cdot\boldsymbol{T} + i\beta x Y}\chi_L \tag{1.26}$$

$$\psi_R = \psi'_R = e^{i\beta(x)Y}\psi_R. \tag{1.27}$$

Note that (1.22) describe massless gauge bosons and massless fermions. Mass term such as $(1/2)M^2 B_\mu B^\mu$ and $-m\bar{\psi}\psi$ are not gauge invariant and so cannot be added. The requirement of a massless gauge boson is familiar. The electron mass term

$$\begin{aligned} -m_e \bar{e} e &= -m_e \left[\frac{1-\gamma^5}{2} + \frac{1+\gamma^5}{2} \right] e \\ &= -m_e(\bar{e}_R e_L + \bar{e}_L e_R). \end{aligned} \tag{1.28}$$

Since e_L is a nember of an isospin doublet and e_R is a signlet, this term breaks gauge invariance. To generate the particle masses in a gauge invariant way, we must use the Higgs mechanism which so-called "Spontaneous Symmetry Breaking".

We take the simplest example: a $U(1)$ gauge symmetry. First, We have Lagrangian

$$\mathscr{L} = (\partial_\mu \phi)^*(\partial_\mu \phi) - \mu^2 \phi^* \phi - \lambda(\phi^*\phi)^2 \tag{1.29}$$

where the complex scalar field is $\phi = (\phi_1 + i\phi_2)/\sqrt{2}$. (1.29) must be gauge invariant.

$$\phi \to e^{i\alpha(x)}\phi \tag{1.30}$$

$$\partial_\mu \to D_\mu = \partial_\mu - ieA_\mu \tag{1.31}$$

$$A_\mu \to A_\mu + \frac{1}{e}\partial_\mu \alpha. \tag{1.32}$$

The gauge invariant Lagrangian is thus

$$\mathscr{L} = (\partial^\mu + ieA^\mu)\phi^*(\partial_\mu - ieA_\mu)\phi - \mu^2\phi^*\phi - \lambda(\phi^*\phi)^2 - \frac{1}{4}F_{\mu\nu}F^{\mu\nu}. \tag{1.33}$$

If $\mu^2 > 0$, this is just the QED Lagrangian for a charged scalar particle of mass μ. However, here we take $\lambda > 0$, $\mu^2 < 0$ since we want to generate masses by spontaneous symmetry breaking. There is now a circle of minima of the potential $V(\phi)$ in the $\phi_1 - \phi_2$ plane of redius v such that

$$\phi_1^2 + \phi_2^2 = v^2, \qquad v^2 = -\frac{\mu^2}{\lambda}, \tag{1.34}$$

as shown in Figure 1.1. Again we traslate the field ϕ to a minimum energy position, which without loss of generality we may take as the point $\phi_1 = v$, $\phi_2 = 0$. We expand Lagrangian about the vacuum in terms of field η and ξ by substituting

$$\phi(x) = \sqrt{\frac{1}{2}}[v + \eta x + i\xi(x)] \tag{1.35}$$

into (1.29) and obtain

$$\begin{aligned}\mathscr{L}' = &\frac{1}{2}(\partial_\mu \xi)^2 + \frac{1}{2}(\partial_\mu \eta)^2 - v^2\lambda\eta^2 + \frac{1}{2}e^2v^2A_\mu A^\mu \\ &-evA_\mu\partial^\mu\xi - \frac{1}{4}F_{\mu\nu}F^{\mu\nu} + \text{interaction terms}\end{aligned} \tag{1.36}$$

The particle of Lagrangian appers to be a masless boson ξ so called Goldstone boson, a massive scalar η, and a massive vector A_μ. From (1.36), we have

$$m_\xi = 0, \qquad m_\eta = \sqrt{2\lambda v^2}, \qquad m_A = ev \tag{1.37}$$

We have the problem of the occurrence of a massless Goldstone boson. So, Note that

$$\phi = \sqrt{\frac{1}{2}}(v + \eta + i\xi) \simeq \sqrt{\frac{1}{2}}(v + \eta)e^{1\xi/v} \tag{1.38}$$

to lowest order in ξ and we substitute a different set of real field h, θ, A_μ, where

$$\phi \to \sqrt{\frac{1}{2}}(v + h(x))e^{i\theta(x)/v} \tag{1.39}$$

$$A_\mu \to A_\mu + \frac{1}{ev}\partial_\mu\theta \tag{1.40}$$

into the (1.36). We obtain

$$\begin{aligned}\mathscr{L}'' = &\frac{1}{2}(\partial_\mu h) - \lambda v^2h^2 + \frac{1}{2}e^2v^2A_\mu^2 - \lambda vh^3 - \frac{1}{4}\lambda h^4 \\ &+\frac{1}{2}e^2A_\mu^2h^2 + ve^2A_\mu^2h^2 - \frac{1}{4}F_{\mu\nu}F^{\mu\nu}.\end{aligned} \tag{1.41}$$

The Glodstone boson acutually does not apper in the theory. The Lagrangian describes just two interacting massive particles, a vector gauge boson A_μ and a massive scalar h which so called a Higgs particles. This is called the "Higgs mechanism". Return for Electrweak sector, we want to formulate the Higgs mechanism so that the $W^\pm$ and Z^0 become massive and the photon remains massless. To do this, we introduce four real scalar fields ϕ_i. The most economical choice is to arrange four fields in an isospin doublet

$$\phi = \begin{pmatrix} \phi^+ \\ \phi^0 \end{pmatrix} = \frac{1}{\sqrt{2}}\begin{pmatrix} \phi_1 + i\phi_2 \\ \phi_3 + i\phi_4 \end{pmatrix}. \tag{1.42}$$

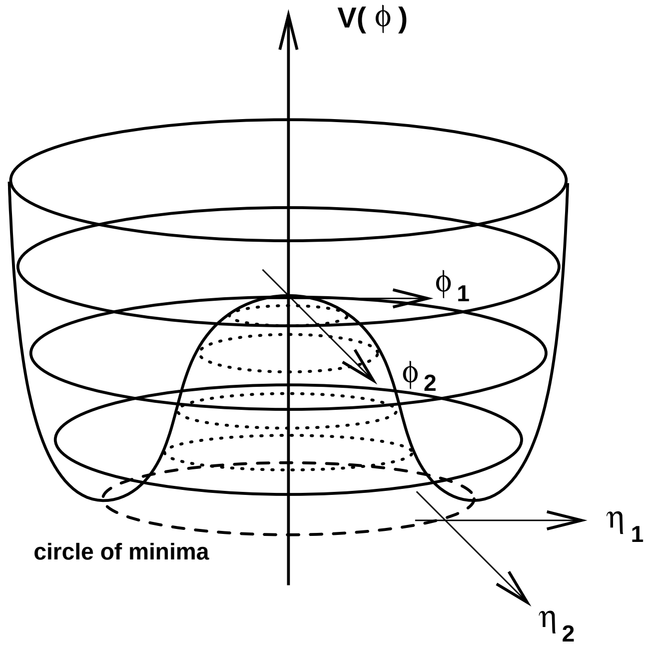

Figure 1.1: The higgs potential V for a cpmplex scalar field with $\nu^2 < 0$ and $\lambda > 0$.

And we must to add to (1.22) an $SU(2)_L \otimes U(1)_Y$ gauge invariant Lagrangian for scalar fields

$$\mathscr{L}_2 = \left| \left(i\partial_\mu - g\boldsymbol{T} \cdot \boldsymbol{W}_\mu - g' \frac{Y}{2} B_\mu \right) \right|^2 - V(\phi) \tag{1.43}$$

It is called the "Weinberg-Salam model". To generate gauge boson masses, we use the Higgs potential $V(\phi)$ with $\mu^2 < 0$, $\lambda > 0$ and choose a vacuum expectation value ϕ_0 of $\phi(x)$.

$$\phi = \sqrt{\frac{1}{2}} \begin{pmatrix} 0 \\ v \end{pmatrix} \tag{1.44}$$

The gauge boson masses are identified by substituting (1.44) in (1.43). The relevant term in (1.43) is

$$\begin{aligned} \left| \left(-i\frac{g}{2}\boldsymbol{\tau} \cdot \boldsymbol{W}_\mu - i\frac{g'}{2} B_\mu \right) \phi \right|^2 &= \frac{1}{8} \left| \begin{pmatrix} gW_\mu^3 + g'B_\mu & g(W_\mu^1 - iW_\mu^2) \\ g(W_\mu^1 + iW_\mu^2) & -gW_\mu^3 + g'B_\mu \end{pmatrix} \begin{pmatrix} 0 \\ v \end{pmatrix} \right|^2 \\ &= \frac{1}{8}[(W_\mu^1)^2 + (W_\mu^2)^2] + \frac{1}{8} v^2 (g'B_\mu - gW_\mu^3)(g'B_\mu - gW^{3\mu}) \\ &= \left(\frac{1}{2} vg \right)^2 W_\mu^+ W_\mu^- + \frac{1}{8} v^2 (g'B_\mu - gW_\mu^3)(g'B_\mu - gW^{3\mu}) \end{aligned} \tag{1.45}$$

where $W^\pm = (W^1 \mp iW^2)/\sqrt{2}$. And we take

$$A_\mu = \frac{g'W_\mu^3 + gB_\mu}{\sqrt{g^2 + g'^2}} \tag{1.46}$$

$$Z_\mu = \frac{gW_\mu^3 - g'B_\mu}{\sqrt{g^2 + g'^2}}. \tag{1.47}$$

From (1.45), we get

$$M_A = 0, \qquad M_W = \frac{1}{2}vg, \qquad m_Z = \frac{1}{2}v\sqrt{g^2 + g'^2}, \tag{1.48}$$

and from M_W, M_A, we get

$$\frac{M_W}{M_Z} = \cos\theta_W \qquad \frac{g'}{g} = \tan\theta_W. \tag{1.49}$$

θ_W is called Weinberg angle or weak mixing angle. It relates the coupling of the electromagnetic and weak interaction accroding to

$$g\sin\theta_W = g'\cos\theta_W = e. \tag{1.50}$$

In term of θ_W, (1.46) and (1.47) therefore become

$$A_\mu = \sin\theta_W W_\mu^3 + \cos\theta_W B_\mu \tag{1.51}$$

$$Z_\mu = \cos\theta_W W_\mu^3 - \sin\theta_W B_\mu \tag{1.52}$$

The mass eigenstates are then autimatically a massless photon (A_μ) and a massive (Z_μ) field with $M_Z > M_W$.

1.2 The Sandard Model Higgs Boson Search

In the Standard Model, the Higgs boson mass is given by $M_{Higgs} = \sqrt{\lambda v^2}$, where λ is the Higgs boson self-coupling parameter. The value of the Standard Model Higgs boson mass is not predicted. However, other thoretical concicerations constrains on the Higgs boson mass. In contrast, the Higgs boson couplings to fermions and gauge bosons are predicted by the theory. The Higgs boson couplings are proportional to the corresponding particle masses, as shown in Figure 1.2. In Higgs boson production and decay processes, the dominant mechanisms involve the coupling of the Higgs boson to the $W^\pm$, Z^0 and the third generation quarks and leptons. Curently, the indirect measurment of the LEP [3] predict that the Standard Model Higgs boson mass is

$$M_{Higgs} = 81^{+52}_{-33} \text{ GeV}/c^2 \tag{1.53}$$

and constrain its value at the 95% confidence level

$$M_{Higgs} < 193 \text{ GeV}/c^2, \tag{1.54}$$

while from the direct measurment, a lower limit of Higgs mass is at the 95% confidence level

$$M_{Higgs} > 114.4 \text{ GeV}/c^2. \tag{1.55}$$

The branching ratios for the dominant decay of the Standard Model Higgs boson are shown in Figure 1.3. For Higgs boson masses below about 130 GeV/c^2, the decay $H \to b\bar{b}$ dominates. However for Higgs boson masses above about 110 GeV/c^2, the decay mode $H \to WW$, where at least one of the W bosons is off-shell (denoted by WW^*) becomes relevant. Above 135 GeV/c^2, this is the dominant decay mode.

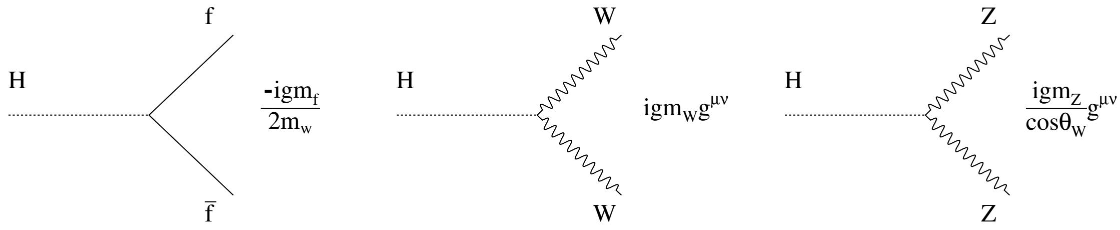

Figure 1.2: Standard Model Higgs boson interactions at tree-level.

We note that the most important Higgs boson production peocesses at the Tevatron. The relavant corss section are shown in Figure 1.4. The most promising Standard Model Higgs boson discovery mechanism at the Tevatron for $M_{Higgs} < 135$ GeV/c^2 consist of $q\bar{q}$ annihilation into the a virtual V^* ($V = W^{\pm}, Z$), where the virtual $V^* \rightarrow VH$ followed by $H \rightarrow b\bar{b}$ and the leptonic decay of the V. In this case, the leptonic decays of final stste W and Z serve as a trigger for the VH events and significantly reduce QCD backgrounds. The detection of Higgs boson siganl is hampered by hadronic decays of W and Z. For the $M_{Higgs} > 135$ GeV/c^2, the Higgs boson decay mode $H \rightarrow WW$ becomes dominant. In this case, the final state consist of three gauge bosons, VWW, and the like-sign dilepton signature becomes the primary signature for Higgs boson discovery. This is the signature of our analysis.

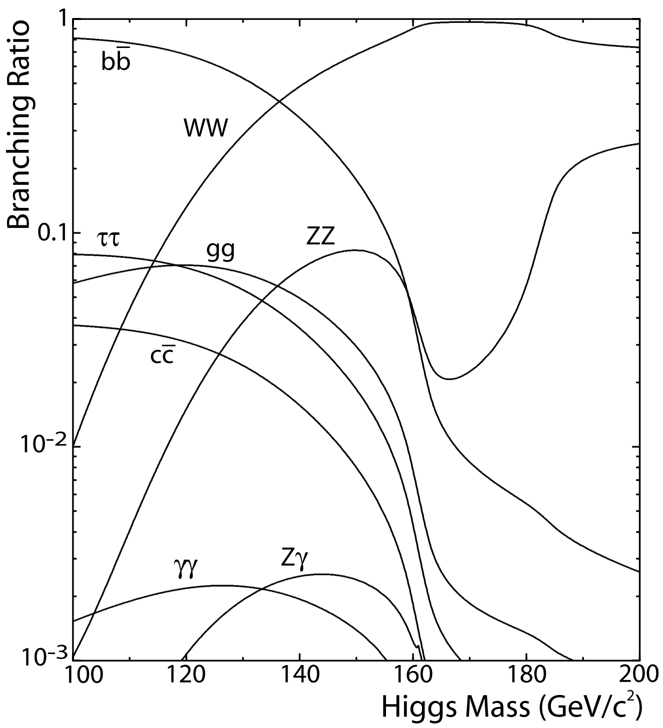

Figure 1.3: Branching ratios of the dominant decay modes of the Standard Model Higgs boson.

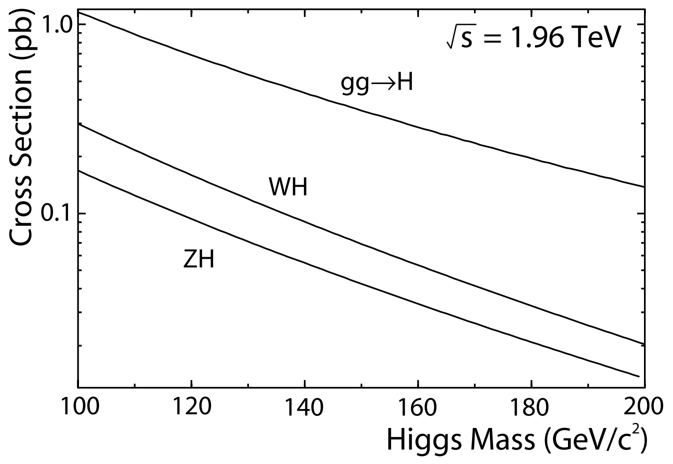

Figure 1.4: Higgs boson production cross section at the Tevatron for the various production mechnisms.

1.3 The Bosophilic Higgs Boson

The Standard Model Higgs boson is responsible for generating the masses of both the weak vector bosons and the fermions. A Higgs boson associated only with the generation of the weak vector boson masses would be expected to have couplings to the weak vector bosons of Standard Model strength, but suppressed coupling to fermions. We will refer to such a particle as a "bosophilic" or "fermiophobic" Higgs boson. The bosophilic Higgs boson can arise in 2 Higgs doublet model (2HDM). Since the fermionic decay modes of a bosophilic Higgs boson are greatly suppressd, the decay of a bosophilic Higgs boson of mass less than $2M_W$ is not dominated by $H \to b\bar{b}$. The branching ratio of a bosophilic Higgs boson decay is shown in Figure 1.5.

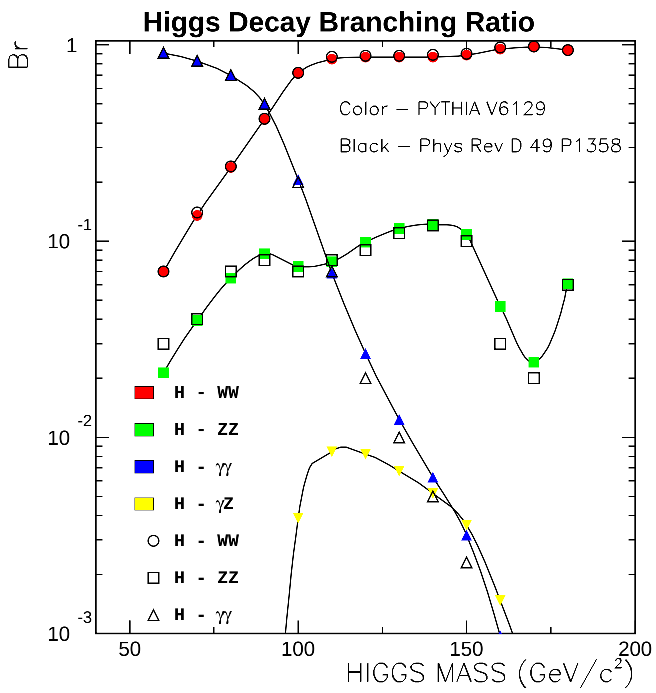

Figure 1.5: Branching ratio of a bosophilic Higgs boson decay.

1.4 Physics Motivation and Previous Result

We once searched for the neutral Higgs boson production in the CDF Run-II data corresponding to an integrated luminosity of 193.5 pb^{-1} in the following decay mode,

$$qq' \to W^{\pm}H \to W^{\pm}W^{*}W^{*} \to \ell^{\pm}\nu\ell^{\pm}\nu + X.$$

The relevant Higgs boson mass region is above 160 GeV/c^2 for the Standard Model Higgs boson where the branching fraction of $H \to WW$ supersedes that of $H \to b\bar{b}$. However, the search for this signature in the region at low mass is important because we need to investigate various Higgs boson couplings as an essential test to convince that signals are attributed to the Higgs boson production as we expect. This channel also covers the case beyond the Standard Model that the Higgs boson couples only to the gauge bosons, which is referred to as the bosophilic Higgs boson. On the experimantal side, the like-sign dilepton event is one of the cleanest signature in hadron collisions. This analysis is therefore expected to have a high potential of the sensitivity for the search of Higgs boson. In the previous analysis, we set cross section upper limits at the 95% confidence level

$$\sigma(WH) \times Br(H \to WW) < 12 \text{ pb for } 100 \text{ GeV}/c^2$$
$$\sigma(WH) \times Br(H \to WW) < 8 \text{ pb for } 160 \text{ GeV}/c^2.$$

Previous result is shown in Figure 1.6. The Standard Model Higgs boson cross section at CDF RunII are also shown in Figure 1.7. In particular, this study is validation of lepton selection cut efficiency and scale factor for $WH \to WWW$ analysis.

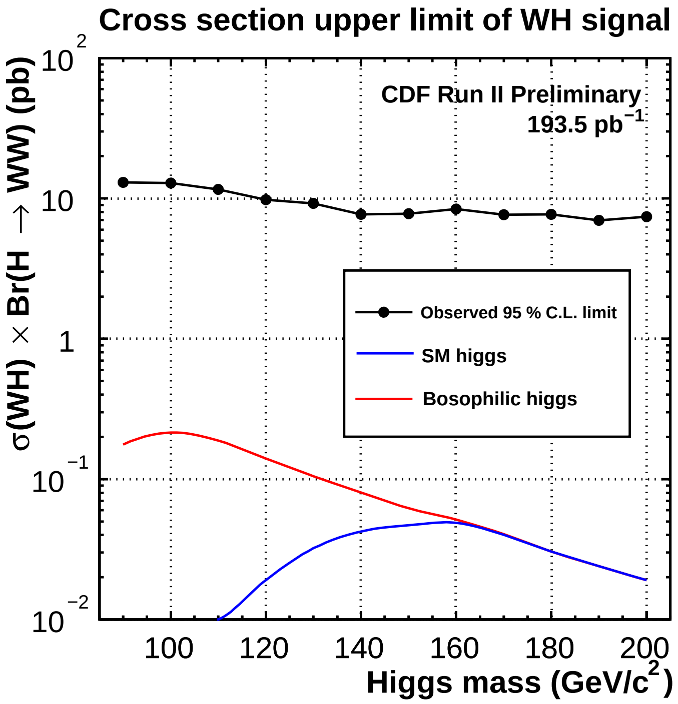

Figure 1.6: Previous cross section upper limit at 95 % confidence level as a function of Higgs boson mass.

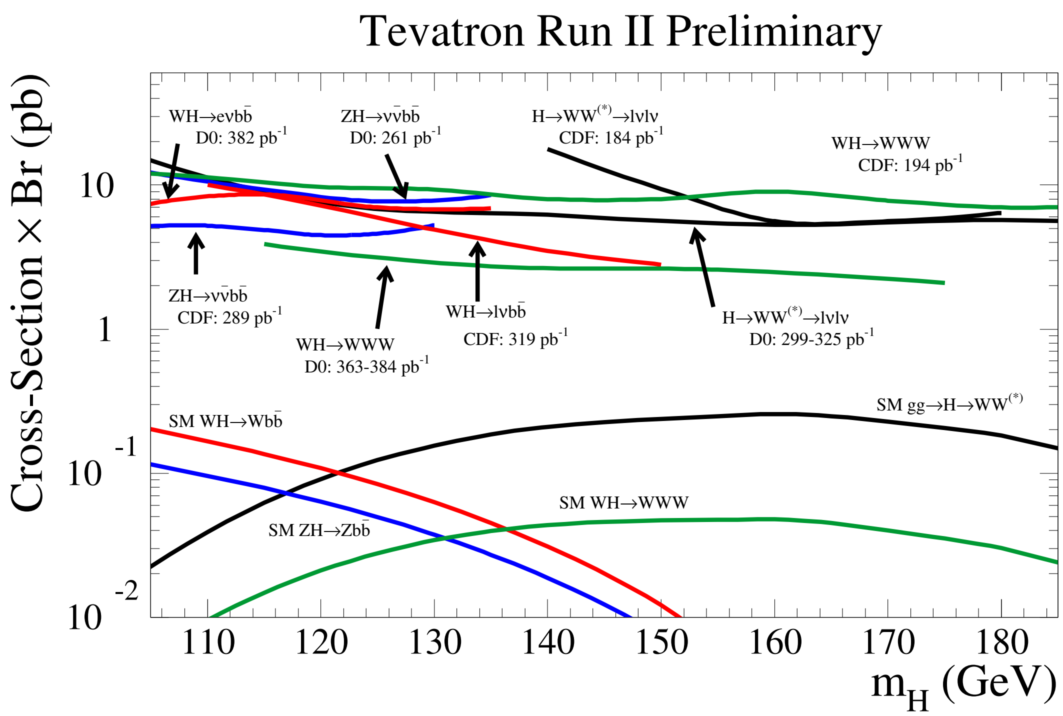

Figure 1.7: CDF Run II preliminary cross section limit for the Standard Model Higgs boson.

Chapter 2

The Experiment Apparatus

The detector used for this analysis is the Collider Detector at Fermilab(CDF) located at the Fermi National Accelerator Laboratory (FNAL). This detector is provided data by proton-antiproton collsions at $\sqrt{s} = 1.96$ TeV. This energy is the highest in the detector in the world. In this chapter, the CDF is described.

2.1 The Tevatron

The Tevatron is a circular acceleator of about 1 km of radius(synchrotron), which collides bunch of protons and antiprotons with spacing of 396 ns. Their bunch move to oppotsite direction, and are accelerated to energy of 0.98 TeV, so a total center of mass energy reaches 1.96 TeV.
The liminosity is given by

$$L = \frac{\gamma}{2\pi} f_0 N_p N_{\bar{p}} B \frac{H}{\beta^*(\varepsilon_p + \varepsilon_{\bar{p}})} \tag{2.1}$$

where γ is the relativistic energy factor, f_0 is the revolution frequency, N_p and $N_{\bar{p}}$ are the number of protons and antiprotons per bunch, B is the number of bunches of each type, β^* is beta function at the center of the interaction region, ε_p and $\varepsilon_{\bar{p}}$ are the proton and antiproton 95% normalized emittances,

2.1.1 Proton Beam

The creation of proton beam begins as a collection of H^- ions produced by ionizing hydrogen gas [4]. The hydrongen molecules are split electrostatically within a cesium-walled chamber. The ions are electrostaically accelerated to a kinetic energy of 750 keV with a Cockcroft-Walton preaccelerator. The Cockcroft-Walton is capacitor-diode voltage multiplying array. On the next, the ions are transmitted to a 150 m long linear accelerator (Linac) consiting of series of drift tubes with radio-frequency cavities [5]. The ions are separated into several bunches, and at the end of the Linac, the ions beam passes through a carbon foil which removes the electrons, and then The bare proton beam reaches a kinetic energy of 400 MeV. The beam enters the booster which is a 150 m diameter synchrotron, and are accelerateed to 8 GeV. Next, The beam enters the Main Injector which is a synchrotron and a major part of the Run II upgrade. The Main Injector accelerate the beam to 150 GeV. Last, the beam enters the Tevatron which is superconducting synchrotorn. The Tevatron accelerates the beam to 980 GeV.

2.1.2 Antiproton Beam

The creation of an antiproton beam begins with the Main Injector. To create an antiproton, the Main Injector accelerates proton beam to 120 GeV, and bump proton beam into a nikel target, then crate a spray of particles which have a small number of antiprotons. This spray of particles is foucsed by s cylindrical lithium lens with 0.5 MA pulsed axial current. The particles are then filtered by a pulsed dipole magnetic spectrometer resulting in an 8 GeV antiproton beam. The antiproton beam is directed to the debuncher, and is temporarily stored in the accumulator until enough antiprotons are collected. The accumulator uses stochastic cooling to reduce the emittance of the beam. The beam enters the Main Injector and is accelerated to 150 GeV. Last, the beam enters the Tevatron and this is accelerated to 980 GeV.

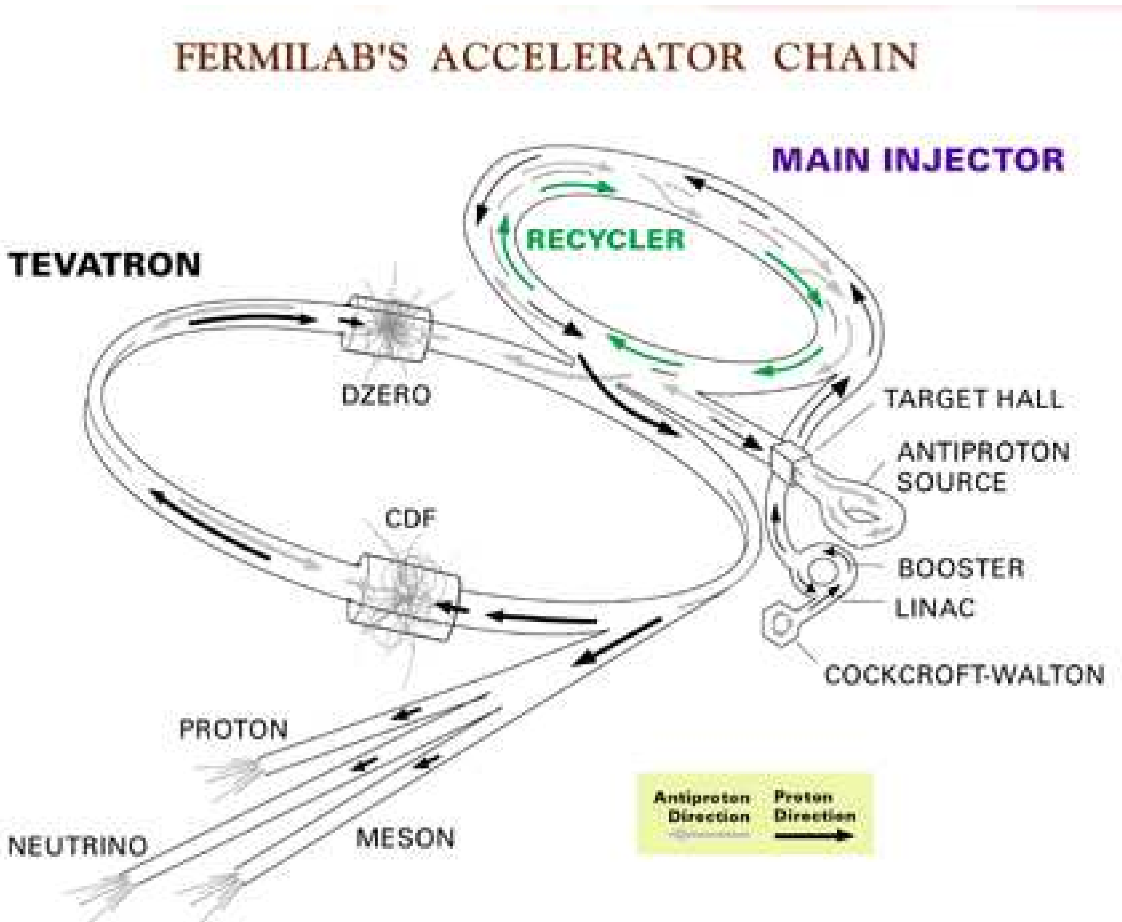

Figure 2.1: The Tevatron Accelerator chain.

2.2 The Collider Detector at Fermilab

The Collider Detector at Fermilab (CDF) is a general purpose detector designed to make pricise position, momentum and energy measurments of particles orignating from the proton and antiproton collisions. An elevation view of the detector is illustrated in Figure 2.2, and a cut away view of the one is in Figure 2.3. The detector is cylindrically symmetric around the beam axis and forward-backward symmetric about the interaction region. This section describes the CDF detector.

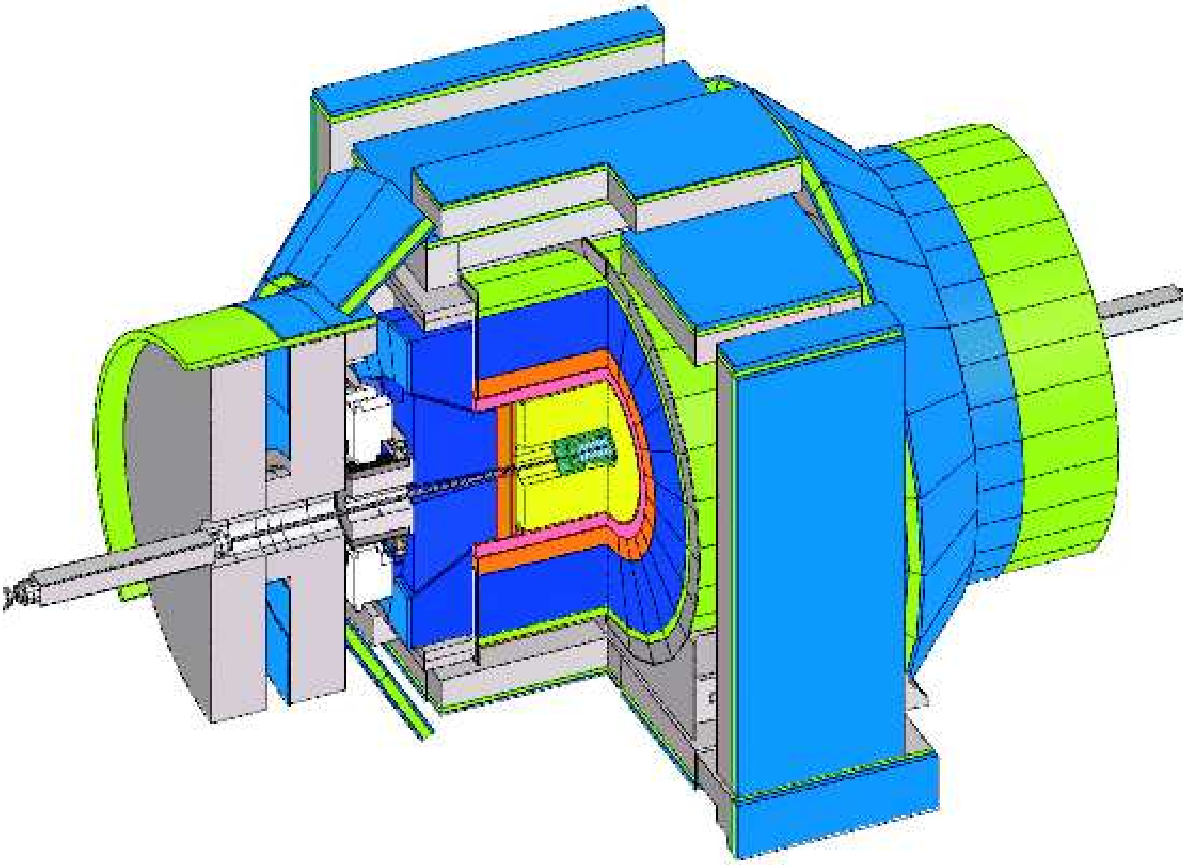

Figure 2.2: Cut away view of the CDF Run II detector.

2.2.1 The CDF Coordinate System

In the CDF detector, a right handed coordinate system is used. The z-axis of the detector coincides with the direction of the proton beam and defines the polar angle θ of the laboratory frame. The x-axis is oriented horizonally away from the detector and y-axis is vertical pointing up-wards. The high energy collisions occurring at the center of the detector produce particles that are uniformly distributed at the azimuathal angle ϕ. The proton and antiproton beam is circulating in the Tevatron are unpolarized, and bunches exhibit a longitudinal density profile such that the resulting distribution of collisions along the beam axis is Gaussian, with a width of about 30 cm. The interested event is that the proton and the antiproton undergo a so-called "hard-scattering" interaction, where thier annihilation produces new particles at high transverse momentum. The center of mass system (CMS) of this hard interaction usually has a boost along the z-axis. Many of the particles produced in the collision, i.e. the remanent proton not participating in the hard scattering interaction, escape down the beam pipe. It is natural to use the rapidity y at hadron colliders as the multilicity of high energy particles

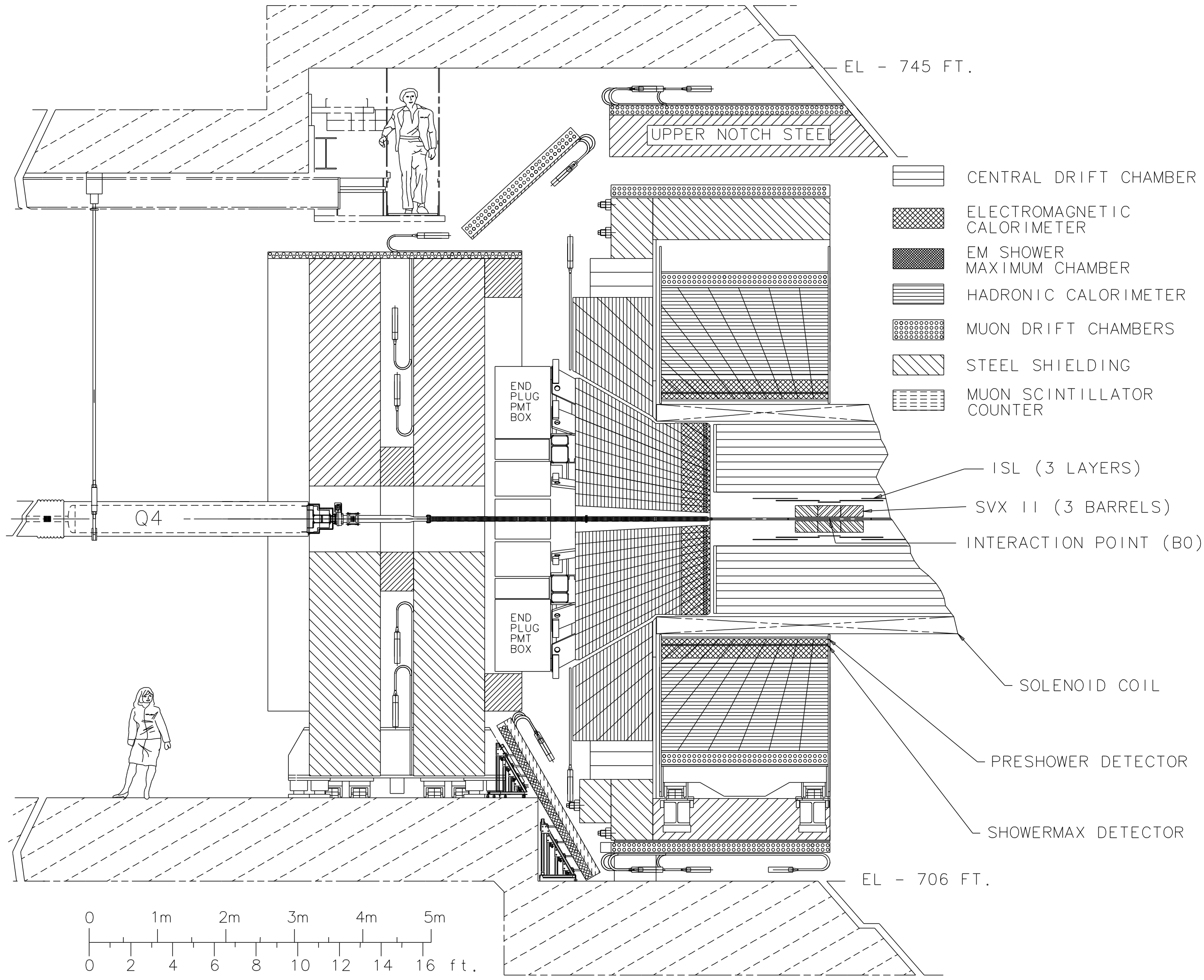

Figure 2.3: Elevation view of one half of the CDF II detector.

is covariant under Lorentz transformation along the z-axis. The rapidity of particle is define as

$$y \equiv \frac{1}{2}\ln\left(\frac{E+p_z}{E-p_z}\right), \tag{2.2}$$

where E is the energy of the particle and p_z is its longitudinal momentum. Particle production is empircally observed to be essentially flat in the rapidity. if a particle is that its momentum much greater than its rest mass, the rapidity is approximately equivalent to

$$\eta = -\ln\left(\tan\frac{\theta}{2}\right). \tag{2.3}$$

This is pseudorapidity. So, the pseudorapidity is equivalent to rapidity for massless particles and is exprimentally convenient as a coordinate because the polar angle is easily measured within the detector.

2.2.2 Charged Particle Tracking Systems

Charged particle tracking plays a major role in almost every physics analysis, done with the CDF detector. The tracking system in CDF, shown in Figure 2.4, consists of open cell drift chamber, the Central Outer Tracker (COT), which covers the region $|\eta| < 1$, and the sillicon inner tracker system, which covers the region $|\eta| < 2$. These tracking systems are immersed in a magnetic field of 1.4 Tesla, produced by a superconduting solenoid niobium-titanium alloy. The magnetic field enables measurements of charge and momentum via the tracking detectors.

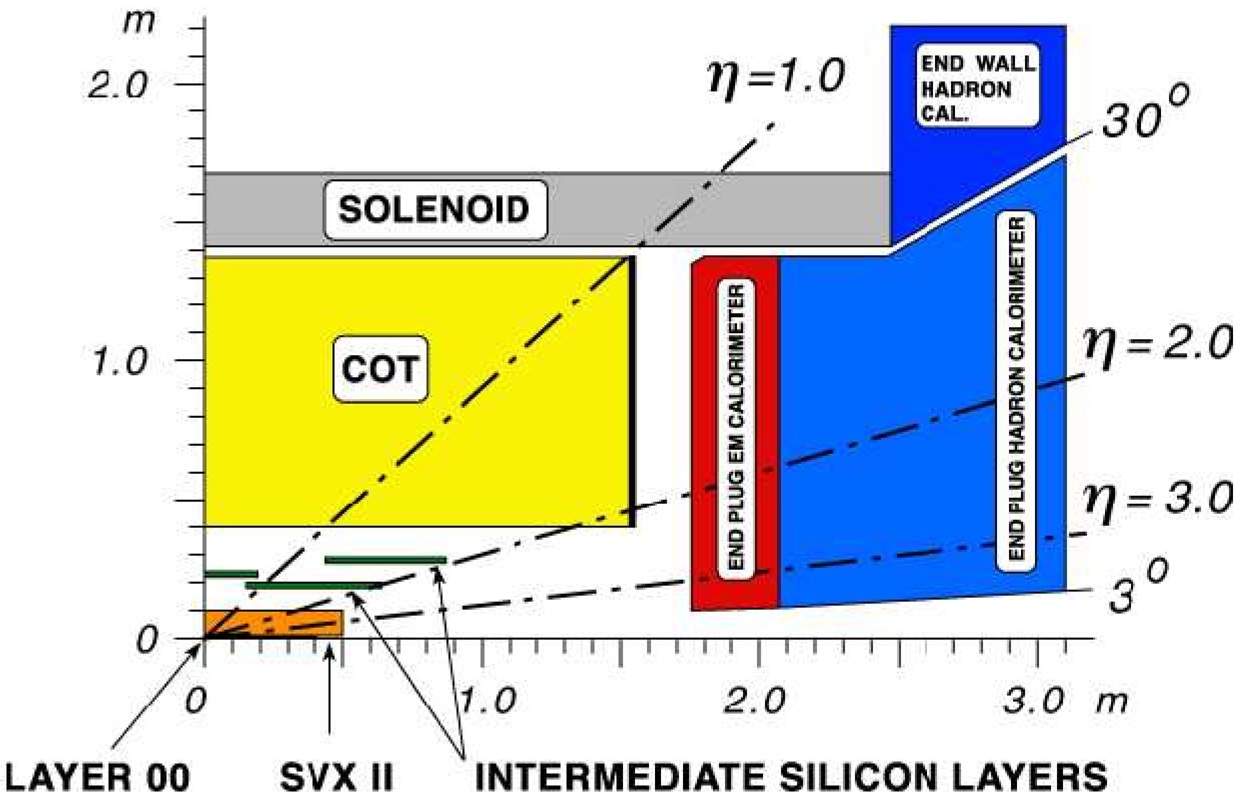

Figure 2.4: Longitudinal view of the CDF tracking system, represnting quarter of the detector.

Silicon Detectors

The sillicon inner tracker consists of three concentric sillicon micro-strip device which provides precise r, ϕ and z tracking information close to the interaction point. The $r-\phi$ view of the sillicon detectors are shown in Figure 2.5.

The innermost one, Layer 00 (L00), is a single-side, radiation-hard sillicon layer located at 1.35 cm radius, just outside the beam pipe, which is located between the radii of 0.83 and 1.25 cm [6].

The Sillicon Vertex Detector (SVX)[7], placed immediately out side L00 at the dadius of 1.6 cm, is composed of three cylindrical barrels with a total length of 96 cm, as shown in Figure 2.6. They extand about 45 cm in the z direction on each side of the interaction point. Each barrel is divided into 12 wedges in ϕ, and each wedge supports five layers of double-sided sillicon micorstrip detectors between the dadii of 2.4 and 10.7 cm from the beam line, to cover the region $|\eta| < 2$. Three of the layers combine the $r-\phi$ measurement on one side with a 90° stereo measurement on the other. The remaining two layers combine the $r-\phi$ measurment in inae side, with a small stereo angle of 1.2° on the other. The stereo angle information from all the layers is combined to form a three dimensional track. A highly parallel fiber-based data acquisition system reads out the entire detetor in approximately 10 μs. Table 2.1 shows the design parameters of the SVX.

The Intermediate Sillicon Layers (ISL) ues a similar technology to that of SVX, from the sillicon itself, through the readout electronics. In the central region layer of double sided sillicon is placed at a radius 22 cm, while in forward region, $1.0 \geq |\eta| \geq 2.0$, two layers of double sided sillicon are placed at radii of 20 cm and 28 cm, where the coverage from the COT is incomplete or missing. Precision space point measuremnts at these radii will enable three dimensional track finding in the forward region. The best position resolution acheved is 9 μm which is for two-strip clusters in SVX II.

SVX	
Readout coordinates	$r-\phi$; $r-z$
Number of barrels	3
Number of layers per barrel	5
Number of wedges per barrel	12
Ladder length	29.0 cm
Combined barrel length	87.0 cm
Layer geometry	staggered radii
Radius innermost layer	2.44 cm
Radius outermost layer	10.6 cm
$r-\phi$ readout pith	60; 62; 60; 60; 65 μm
$r-z$ readout pith	141; 125.5; 60; 141; 65 μm
Length of readout channel($r-\phi$)	14.5 cm
$r-\phi$ readout chips per ladder	4; 6; 10; 12; 14
$r-z$ readout chips per ladder	4; 6; 10; 8; 14
$r-\phi$ readout channels	211, 968
$r-z$ readout channels	193, 536
Total number of channels	405, 504
Total number of readout chips	3, 168
Total number of detectors	720
Total number of ladders	180

Table 2.1: Design parameters of SVX detector at CDF.

Central Outer Tracker

The Central Outet Tracker (COT) [8] has played a major role in charged particles tracking as CDF. It is an open-cell drift chamber which provides coverage for the region

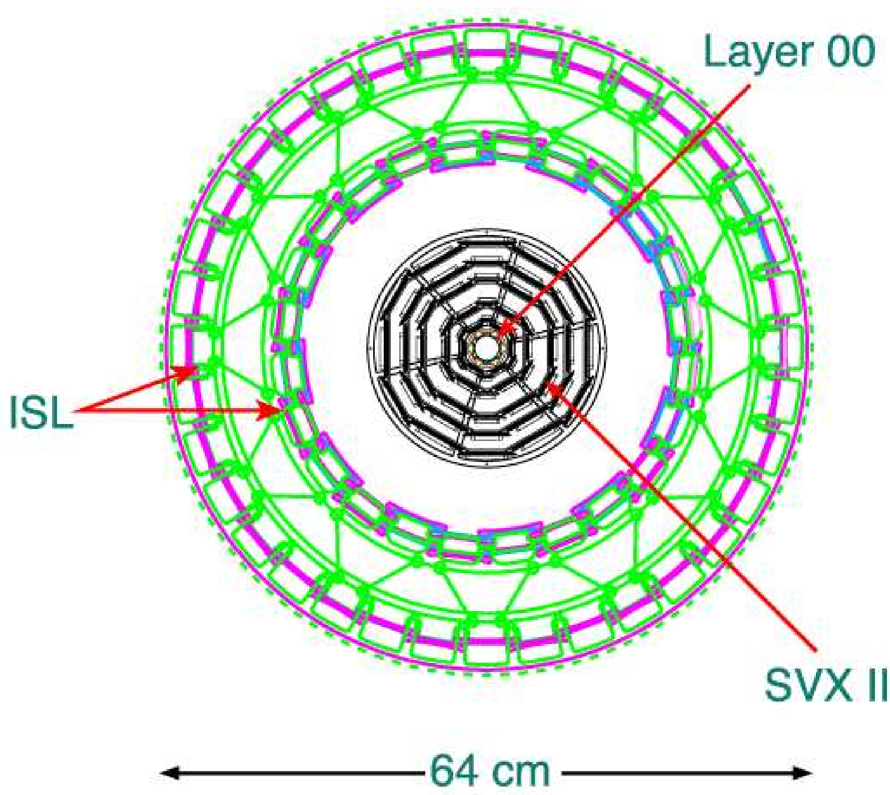

Figure 2.5: $r - \phi$ view of the silicon detectors.

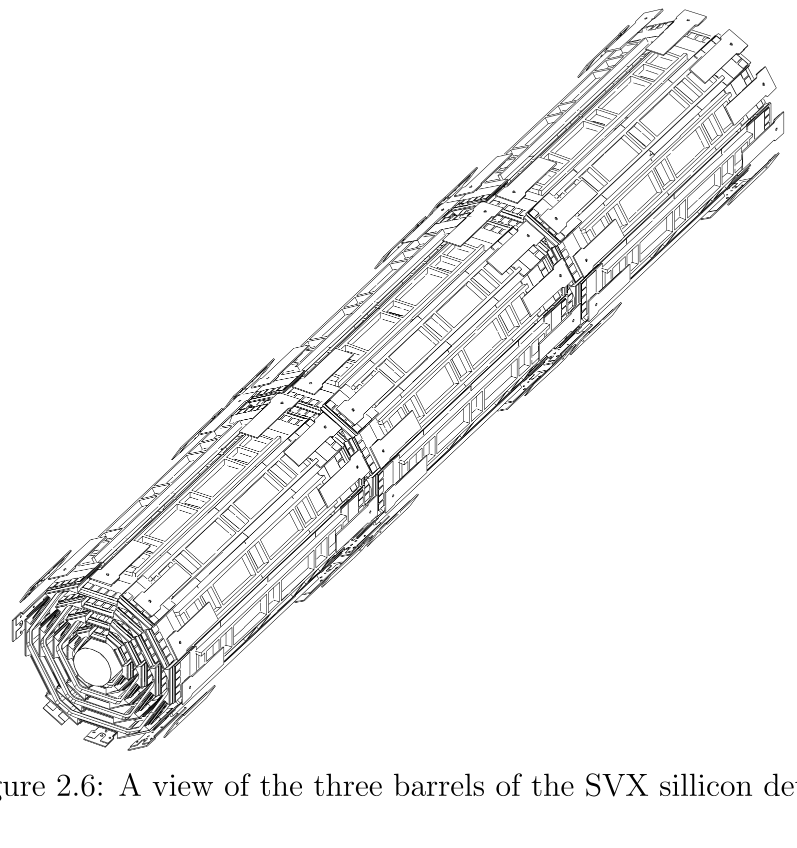

Figure 2.6: A view of the three barrels of the SVX sillicon detector.

$|\eta| < 1$ as shown in Figure 2.4. The COT consists of eight superlayers of cells placed between the radii of 40 cm and 132 cm from beam pipe. Each superlayer is compased of 12 layers of sense wires alternated with potential wires in a plane, as shown in Figure 2.7. The space between the cells is filled with a gas mixture of Argon and Ethane in the proportions 50 : 50, chosen to ensure a fast drift velocity ($\sim$ 100 μm/ns) in order to deal with the expected high luminosity. Four of the superlayers are axial (for the measurements in the transvrese plane) and the other four are stereo (for the z measurements), with stereo angles of $\pm$ 2 degree; the superlayers are alternated starting with a stereo superlayer. A summary of COT characteristics is given in Table 2.2. The ions produced by a chrged particle passing through the COT are collected at the sense wires giving the $r - \phi$ information on the position of hits. The hits from the stereo and axial wires are combined to obtain the z position. The three dimensional from the curvature in the magnetic field. If B is the strength of the magnetic field, the transverse momentum p_T of the track can be obtained by the relationship

$$p_T = Bqr, \tag{2.4}$$

where q is the charge of the particle and r is the radius of curvature of the track. The rasolution on the curvature has been studied using detailed simulation and has been found to be 0.68×10^{-4} cm^{-1} which corresponds to a momentum resolution $\sigma p_T/p_T^2$ $\sim 3 \times 10^{-3}$ GeV/c^{-1}. As more energetic tracks bend less, the curvature, and thus the momentum resolution of the COT, decreases for higher momentum tracks. The resolution on the impact parameter d_0 is about 600 μm, the resolution on $\cot\theta$ is $\sim 6 \times 10^{-3}$.

COT	
Number of Layers	96
Number of Superlayers	8
Stereo Angle (degree)	+2, 0, −2, 0, +2, 0, −2, 0
Layers per Superlayer	12
Rapidity Coverage	$\|\eta\| < 1$
Drift field	2.5 keV/cm
Maximum Drift Distance	0.88 cm
Maximum Drift time	177 ns
Number of Channels	30, 240
Material Thickness	1.6% X_0

Table 2.2: Design parameters of COT detector at CDF.

2.2.3 Calorimeters

Located outside the solenoid, the calorimatry system is used to measure the energy of charged and neutral particles, which covers the region $|\eta| < 3.0$. The calorimeter is divided in to two physical sections, central ($|\eta| < 1$) and plug detector ($1.1 < |\eta| < 3.6$). Each sections is subdivied into an electromagnetic (CEM, PEM) and hadronic (CHA, PHA). The endwall hadronic calorimater (WHA) covers a gap between the cantral and plug hadronic sections, as shown in Figure 2.4.

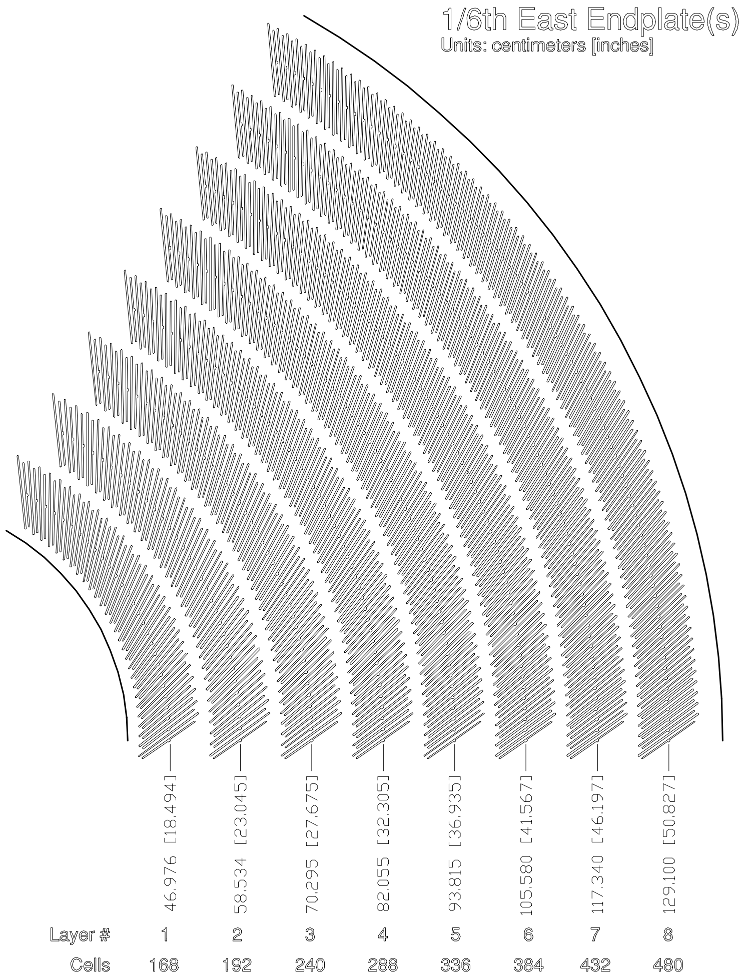

Figure 2.7: 1/6 section of the COT end plate. For each superlayer is given the total number of supercells, the wire orientation (axial or stereo), and the average radius.

Central Calorimeters

The Central Electromagnetic Calorimeters (CEM) [10] is a sampling calorimater made of lead sheets interspersed with polystyrene scintillator. It detects electrons and photons and measures thier energy. While other particles that interact electromagnetically may also deposit some of their energy in the CEM, electrons and photons deposit almost all of their energy in the calorimeter. The CEM total thickness is 18 radiation length (32 cm), to make sure that 99.7 % of the electrons energy will be deposited. The shower topology information allows us to distinguish an electrons a photon from a light hadron (π or K) or muon signals that may also shower in the calorimeter, since the transverse development of the showers is different for these particles. While passing through the calorimeter, particles interact with the material producing 'showers' of photons, electrons and positrons depending on thier nature. Electrons and photons will start showering eariler and thier showers will be almost constrained to the EM sections, while hadrons (such as pions) in the form of hadronic jets will start later releasing a significant fraction of their energy in the hadronic portions.

A proportional strip chamber (CES) is inserted into the stacks between the 8th layer of lead and the 9th layer of scintillaltor. The location is at depth of 6 raditation lengths, and corresponds to the longitudinal shower maximum. The CES chambers consists of crossed anode wires and cathode strips. The wires run along z spaced at 1.45 cm and mearsure the azimuthal position of the electromagnetic shower within the CEM wedge. The cathode strips run on the ϕ direction and measure the z position of the shower. The cathode spactng is 1.67 cm in towers zero through four, and 2.01 cm in towers five through nine. The CEM has an average energy resolution

$$\frac{\sigma(E)}{E} = \frac{14.0\%}{\sqrt{E_T}} \oplus 2\% \tag{2.5}$$

where E_T is the transverse energy of the detdected particle in GeV, $\oplus$ denotes addition in quadrature. The position resolution is 2 cm at 50 GeV. A second set of proportional chamber, the Central Preradiator (CPR) detector is placed in between the front face of the EM calorimeters and the magnet coil. This chamber can be very useful in the pion-photon separation and in the identification of the electrons.

The CHA (Central Hadron) is an iron-scintillator sampling calorimeter, approximately 4.5 λ_0 (interaction lengths) in depth, and has

$$\frac{\sigma(E)}{E} = \frac{50.0\%}{\sqrt{E_T}} \oplus 3\% \tag{2.6}$$

The WHA (Wall Hadron) is also an iron-scintillator sampling calorimeter, spanning a range in pseudorapidity of $0.7 < |\eta| < 1.3$. The WHA has a depth of about 4.5 λ_0, similar to the CHA, however it has worse energy resolution,

$$\frac{\sigma(E)}{E} = \frac{75.5\%}{\sqrt{E_T}} \oplus 4\% \tag{2.7}$$

Plug Calorimeters

The plug upgrade calorimeter covers the polar angle region from 3° to 37° ($1.1 < |\eta| < 3.6$). The top half of one plug is shown in cross section in Figure 2.8. Each plug wedge spans 15° in azimuth, however from $1.1 < |\eta| < 2.11$ (37° to 14°) the segmentation in ϕ is doubled, and each tower spans only 7.5°. There is an electromagnetic section (PEM) with a shower position detector (PES), followed by a hadronic section (PHA).

The PEM calroimeter is lead/scintillator sampling type, with unit layers conposed of 4.5 mm lead and 4mm scintillator. There are 23 layers in depth for a total thickness of about 21 X_0 (radiation length) at normal incidence. The PEM has an energy resolution is

$$\frac{\sigma(E)}{E} = \frac{16\%}{\sqrt{E_T}} \oplus 1\% \tag{2.8}$$

The PHA is an iron-scintillator sampling calroimeter, approximately 7 λ_0 in depth, and has an energy resolution of

$$\frac{\sigma(E)}{E} = \frac{80\%}{\sqrt{E_T}} \oplus 5\% \tag{2.9}$$

The PEM shower maximum detector is located about 6 λ_0 deep within the PEM, and is constructed of two layers (denoted 'U' and 'V') of scintillating strips. The strips are 5 mm wide, and roughly square in cross section. Position resolution of the PES is about 1mm.

Calorimeter	CEM	CHA	WHA	PEM	PHA
Coverage	$\|\eta\| < 1.1$	$\|\eta\| < 0.9$	$0.7 < \|\eta\| < 1.3$	$1.1 < \|\eta\| < 3.6$	$1.1 < \|\eta\| < 3.6$
Modules	48	48	48	24	24
η towers / module	10	8	6	12	10
Layers	31	32	15	23	23
Material	Lead	Steel	Steel	Lead	Iron
Radiation Length	19 X_0	4.5 λ_0	4.5 λ_0	21 X_0	7 λ_0
Energy Resolution	$\frac{14.0\%}{\sqrt{E_T}} \oplus 2\%$	$\frac{50.0\%}{\sqrt{E_T}} \oplus 3\%$	$\frac{75.0\%}{\sqrt{E_T}} \oplus 4\%$	$\frac{16.0\%}{\sqrt{E_T}} \oplus 1\%$	$\frac{80.0\%}{\sqrt{E_T}} \oplus 5\%$

Table 2.3: Design parameters of the calorimeter at CDF.

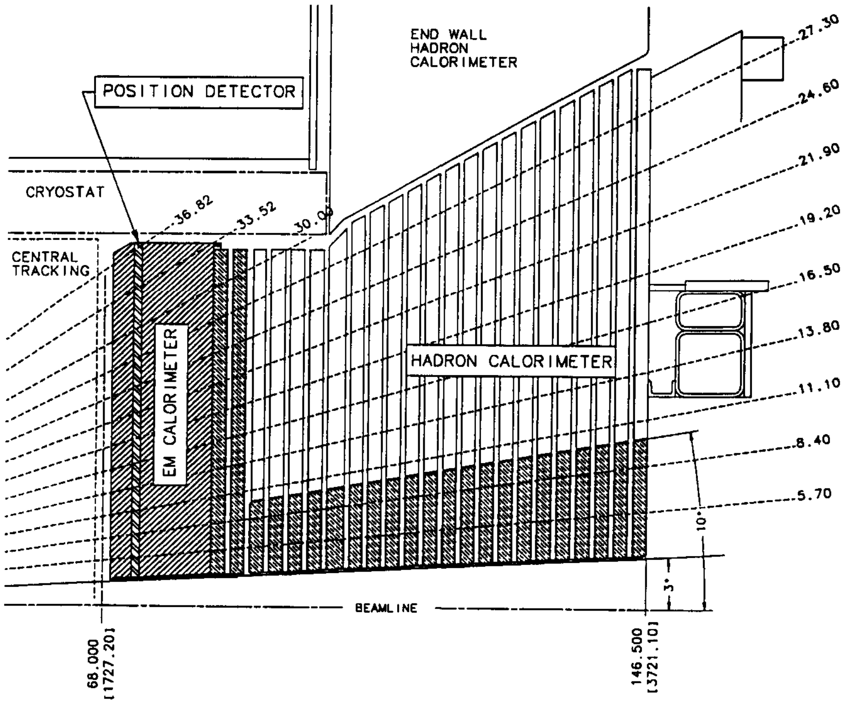

Figure 2.8: The cross section of upper part of the end plug calorimeter.

2.2.4 Muon Chambers

Muons penetrate the tracking systems and the calorimeters leaving very little energy. The reason is muons produce much less bremsstrahlung than electrons and therefore do not produce electromagnetic showers, due to their larger mass. The CDF muon systems [9] use this property by placing detectors behind enough material. Muons deposit minimum ionizing energy in the calorimeters matched with a track in the COT. The momentum of these muons is mearsured by their bend in the solenoidal field using the COT. The central muon system is capable of detecting with transverse momentum p_T ≤ 1.4 GeV, through their interaction with the gas and subsequent drift on the produced electrons toward the anode wires.

The muon systems consist of four separate subsystems: the central muon chambers (CMU), the central upgrade (CMP), the central muon extension (CMX), and the barrel muon detector (BMU). Figure 2.9 shows a plot of the effective muon detector coverage in $\eta - \phi$ space. Table 2.4 shows design parameters of the detector. The CMU detector located directly outside of the central hadron calorimeter, 35 m from the interaction point, and covers the region of $|\eta| \leq 0.6$. It is divided into 24 east and 24 weat 15°-wedges. Each wedge contains three muon chambers and each muon chamber consists of four layers of four rectangular drift cells staggered in order to eliminate hits position ambiguities. A stainless steel sense wire a diameter of 50 μm is loacted in the center of each cell. By comparing sanse wires the muon passed. A muon object is created by forming a “stub” from hits in the muon chambers matching it to an extrapolated COT tracks.

The CMP consists of a second set of muon chambers behind additional 60 cm of steel in the region $55° \leq \phi \leq 90°$. The chambers are fixed length in z and form box around the central detector. The pseudorapidity coverage thus varies with azimuth as shown in Figure 2.9. The inner and outer surfaces of the detector are lines with scintillator planes (CSP) to provide timing information for the trigger system.

The central extension consist of conical section of drift tubes (CMX) and scitillaing in polar angle from 42° to 55° ($0.6 \leq |\eta| \leq 1.0$).

Muon chamber	CMU	CMP/CSP	CMX/CSX	BMU
Coverage	$\lvert\eta\rvert \leq 0.6$	$\lvert\eta\rvert \leq 0.6$	$0.6 \leq \lvert\eta\rvert \leq 1.0$	$1.0 \leq \lvert\eta\rvert \leq 1.5$
Drift tube cross section	1.68×6.35 cm	2.5×15 cm	2.5×15 cm	2.5×8.4 cm
Drift tube length	226 cm	640 cm	180 cm	363 cm
Max drift time	800 ns	1.4 μs	1.4 μs	800 ns
Total drift tubes	2304	1076	2208	1728
Scinitillation counter thickness		2.5 cm	1.5 cm	2.5 cm
Scinitillation counter width		30 cm	30-40 cm	17 cm
Scinitillation counter length		320 cm	180 cm	180 cm
Total counters		269	324	864
Pion interaction length	1.5	7.8	6.2	6.2-20
Minimum detectable muon p_T	1.4 GeV/c	2.2 GeV/c	1.4 GeV/c	1.4-2.0 GeV/c
Multiple scattering resolution	12 cm/p	15 cm/p	13 cm/p	13-25 cm/p

Table 2.4: Design parameters of the muon detectors at CDF. Pion interaction lengths and multiple scattering are computed at s reference angle of $\theta = 90°$ in CMU and CMP/CSP, at an angle of 55° in CMX/CSX, and show the range of values for the BMU.

2.2.5 Luminosity Monitors

CDF monitors the instaneous luminosity of the Tevatron using a Chrenkov Luminosity Counter (CLC) [11]. These are two CLC detector modules in the CDF detector installed in a “3-degree holes” inside the CDF and plug calorimeter, which covers the ragion 3.7 $\leq |\eta| \leq 4.7$. Each CLC module consists of 48 thin, long, conical, gas-filled, Cherenkov counters.

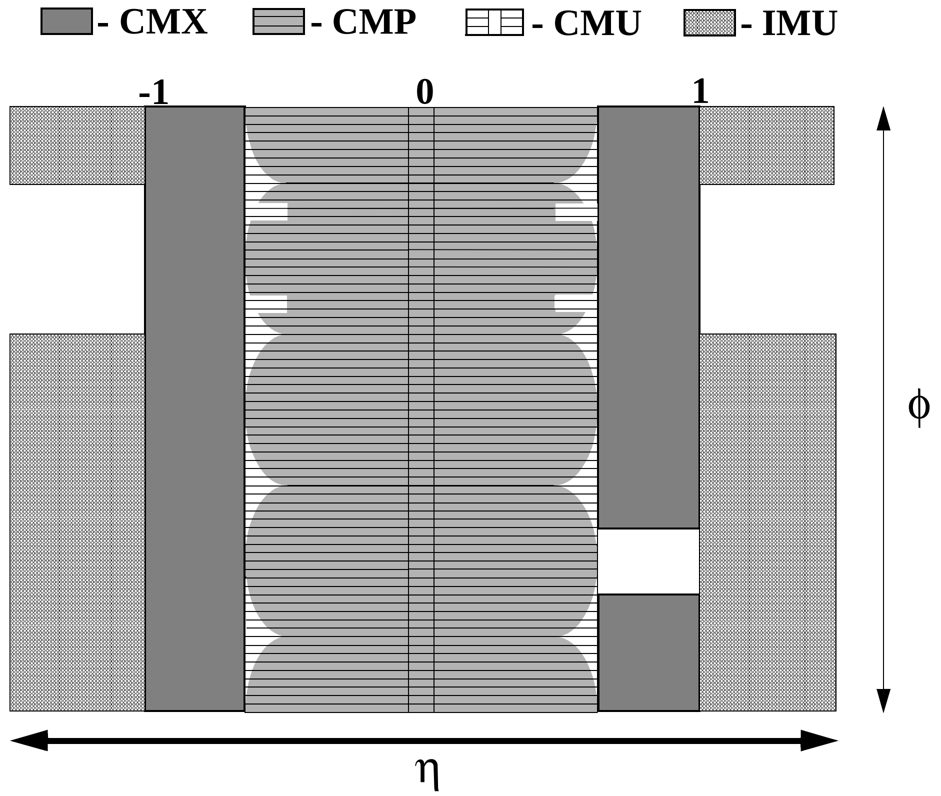

Figure 2.9: Muon detector coverage.

2.3 Trigger Systems

The trigger plays an important role on hadron collider experiment bacause the collision rate is much higher than the rate as which data can be stored on tape. The crossing rate of the Tevatron under 36 on 36 bunch operation is 7.6 MHz, corresponding to 396 ns collision separation. The role of the trigger is to effectively extract the most interesting physics events from the large number of minimum bais events. For Run II, CDF employs a three-level trigger system to selectively capture interesting events. The levels are denoted simply as "L1", "L2" and "L3", with each subsequent level making more complicated decisions and requiring successively longer processing times. Figure 2.10 shows schematic of the CDF trigger system.

2.3.1 Level-1

The first level of trigger selection Level-1 (L1) uses custom designed hardware to find phiysics objects based on a subset of the detector information and then makes a decision based on simple counting of these objects. The input to the L1 hardware comes from the calorimeters, tracking chambers and muon detectors. The decision to retain an event for further processing is based on the number and energies of the electron, jet and muon candidates as well as the missing energy in the event, or on the kinematic properties of few of these objects. The L1 hardware consists of three parallel synchronous processing streams which feed inputs of the single Global Level-1 decision unit. One stream finds calorimeter objects, another finds muons and the third finds tracks in the central region. The L1 trigger can be formed using these streams singularly as well as AND or OR combinations of them. All elements of the L1 trigger are synchronized to the same 132 ns clock, with a decision made every 132 ns by Global L1. In the period of the data taking considered in this analysis the accelerator was the two intermediate clock cycles automatically rejected. The maximum L1 accept rate is 20 kHz, while the typical one is 12 kHz.

2.3.2 Level-2

Events accepted by L1 are proessed by the second level of trigger Level-2 (L2), which is composed of several asynchronous subsystems. These provide input data to programmable L2 processors on the Global L2 crate, which determine if any of the L2 trigger are satified. Processing for L2 trigger decision starts after the event written into one of the four L2 buffers by a L1 accept. When L2 is analyzing the event in one of the buffers, that buffer cannot be used additional L1 accept. If all the four are full, the deadtime of the data acquisition is increased. It follows that the time required for a L2 decision needs to be less than about 80 % of the average time between L1 accepts in order to keep the deadtime as low as possible. For this purpose L2 has been pipelined into two stages each taking approximately 10 μs, which is sufficient to keep the deatime at a minimum, even if L1 had an accept-rate of 50 kHz. The L2 buffers perform a limited event reconstruction using essentially all the information used in L1, but with higher precision. In addition, at L2, data from the central shower-max detector and the SVX are available, which improve respectively the identification of electrons and photons and the reconstruction of the secondary vertices. Furthermore, a jet reconstruction algorithm is provided by the L2 cluster finder. After all of the data are stored in the processors, the event is examined to check if the criteria of any of the L2 triggers have been satisfied. This operation can be performed while the new events are being loaded into memory, thus not affecting the dead time. The typical L2 accept rate, as of this writing, is between 100 and 300 Hz, depending on the initial luminosity.

2.3.3 Level-3

The Level-3 (L3) trigger subsystem is composed of two main components, the Event Builder (EVB) and the Level-3 Farm. Level-1 and Level-2 systems need to make their decisions at very high rate which makes it impossible to fully reconstruct each event. While Level-1 and Level-2 algorithms use small predefined pieces of event data to make their decision, the event pieces are stored in the buffers of the 140 Front End crates which constitute the EVB. After a L2 decision is made, the Event Builder aseembles all event fragments from the Front End crates into one data block.

The 16 subfarms which compose the L3 Farm receive event fragments from the EVB and bulid complete events into the appropriate data structure for analysis. Since it takes about one second for one computer unit to make a trigger decision on one event, it takes a large farm of 250 Dual Pentiun Linux personal computers (called "processors") to ensure the reqired input rate. Each subfarm contains between 14 and 18 processor nodes and one "converter" node, which acts as "farm input " distributing the data flow coming from the EVB.

The events are then passed to a trigger algorithm (a different one for each processor) that categorizes the event and makes the decision as to whether or not to permanently sotre it. The selected event are passed to the Data Logger subsystem. During the building processing, the event integrity is checked. The L3 algorithms take advantage of the full detector information and improved resolution unavailable to lower trigger levels. This includes full three-dimensional track reconstruction and tight matching of tracks to calorimeter and muon-system information. Results from the lower level are used ro drive the algorithms, which are based on the off-line analysis packages. This is a modular and separated filter modules for specific triggers. L3 accept events with a rate of approximately 75 Hz.

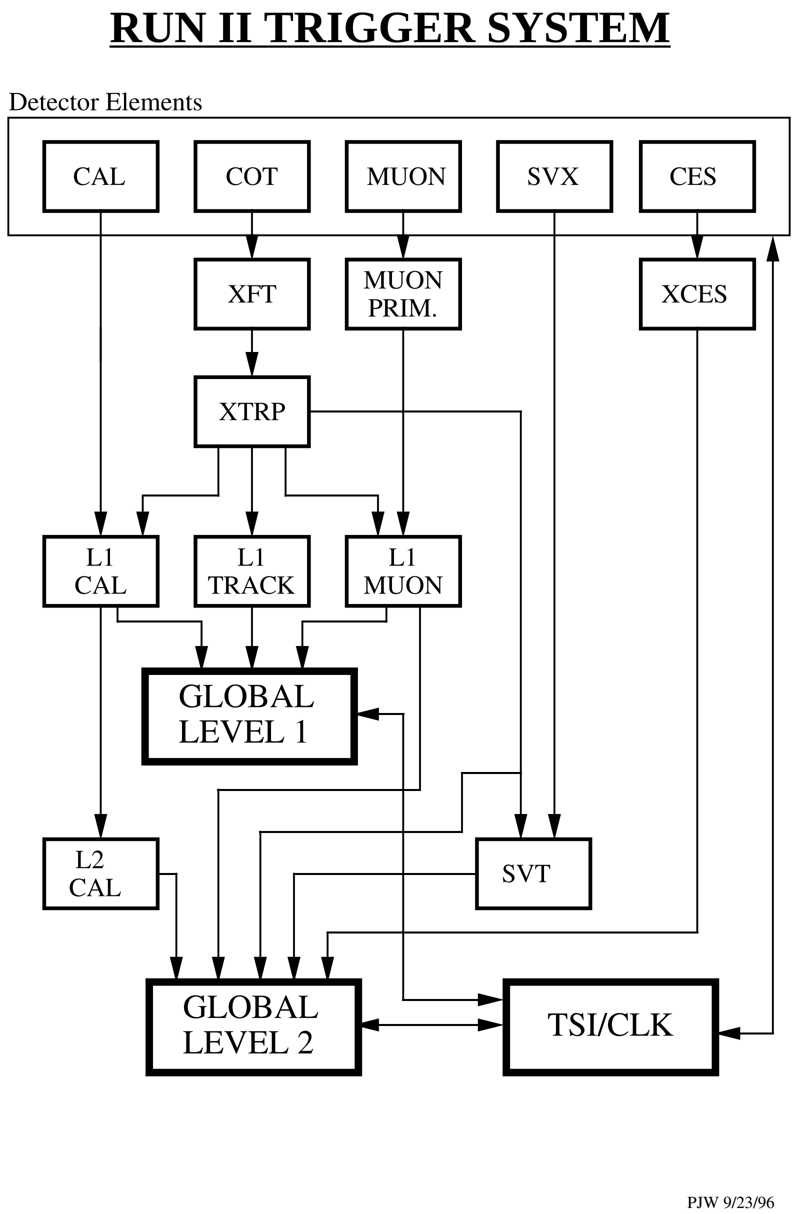

Figure 2.10: Block diagram of the CDF II trigger system.

Chapter 3

Lepton Selection Cut Efficiency and Scale Factor

We study about efficiency for lepton (electron, muon) selection cut and sacle factor. The study is for $WH \rightarrow WWW$ analysis. Since this Higgs event has the final state of like-sign dilepton, we must estimate lepton selection cut efficiency. the efficiency is estimated using $Z \rightarrow \ell\ell$ Data and MC. The Data is high p_T inclusive leptons sample. For electron, Luminosity is 29.44 pb^{-1}, and for muon Luminosity, is 52.40 pb^{-1}. Used MC sample is $Z \rightarrow \ell\ell$. $Z \rightarrow e^+e^-$ is about 100,000 events and $Z \rightarrow \mu^+\mu^-$ is about 200,000 events. The estimated efficiencies are geometrical and kinematical acceptance, isolation cut and identification cuts.

3.1 Lepton Selection Variables

3.1.1 Event Selection Variable

This Event selection variable is to get good events.

- z_{vtx} :

  This variable is the z coordinate of the interaction vertex where the lepton has originated. This vertex is primary vertex on this study.

3.1.2 Electron Selection Variables

The variables are to select the central electrons. The variable is the following.

- Fiduciality :

  This variable ensure that the electron is reconstructed in a region of the detector which well instrumented. The electron position in the CEM is determined using either the value determined by the CES shower or by the extrapolated track, and it must satisfy the following requirements:

  - The electron must lie within 21 cm of the tower center in the $r - \phi$ view in order for the shower to be fully contained in the active region $|c_{\mathrm{CES}}| < 21$ cm.
  - The electron should not be in the regions $|z_{\mathrm{CES}}| < 9$ cm, where the two halves of the central calorimeter meet, and $|z_{\mathrm{CES}}| > 230$ cm, which corresponds to

outer half of the last CEM tower. This region is prone to leakage into the hadronic part of the calorimeter.

- the electron should not be in the region immediately closest to the point penetration of the cryogenic connections to the solenoidal magnet, which is uninstrumented. This corresponds to $0.77 < \eta < 1.0$, $75 < \phi < 90$ degree, and $|z_{\ CES}| < 193$ cm.

- E_T :

  The transverse electromagnetic energy deposited by electron is calculated as the electromagnetic cluster energy multiplied by $\sin\theta$, where θ is the polar angle provided by the best COT track pointing to the EM cluster.

- p_T:

  The transverse momentum of the COT beam constrained track as measured using the track curvature in the COT.

- Isolation :

  This variable is defined by the energy in cone of radius $\Delta R = \sqrt{\Delta\eta + \Delta\phi} < 0.4$ around the cluster excluding cluster.

  $$\mathrm{ISO}^{\mathrm{cal}}_{0.4} = \sum_{\Delta R < 0.4} E_T^{\mathrm{cal}} - E_T^{\mathrm{clust}} \tag{3.1}$$

  where E_T^{clust} is defined by seed tower plus two towers adjacent to the seed tower in η.

- HAD/EM :

  This variable is the ratio of total energy in the hadronic calorimeter to total energy in the electromagnetic calorimeter for cluster.

- L_{shr} :

  The purpose of this quantity is to provide some discrimination of electrons and photons from hadronic showers faking these particles in the central electromagmetic calorimeter. This is done by comparing the observed the energy in CEM towers adjacent to the seed tower to expected electromagnetic shower taken with test beam data.

  $$L_{\mathrm{shr}} = 0.14 \sum_i \frac{E_i^{\mathrm{adj}} - E_i^{\mathrm{exp}}}{\sqrt{(0.14\sqrt{E})^2 + (\Delta E_i^{\mathrm{exp}})^2}} \tag{3.2}$$

  where E_i^{adj} is the measured energy in tower adjacent to the seed tower, E_i^{exp} is the expected energy in the adjacent tower from test beam data, $\Delta E_i^{\mathrm{exp}}$ is the error on the energy estimate.

- E/p :

  This variable is defined by the ratio of the cluster energy to the beam constrained COT track momentum.

- χ^2_{strip} :

  The pulse height shape in the CES(Central Electromagnetic Shower-Max) detector in the $r-z$ view is compared to the obtained with test beam data using the χ^2 test.

- Δx_{CES} and Δz_{CES} :

  These variable are the differences between the x or z coordinates of the track extrapolated to the CES and the value of x or z as measured by CES itself. Δx_{CES} is the separation in the $r-\phi$ view, while Δz_{CES} is the separation in the $r-z$ view. For Δx_{CES} cut, Δx_{CES} is multiplied by the electric charge of electron.

- Track Quality :

  To ensure that the track associated with the electron is good quality reconstructed track, require that track hes been reconstructed in the COT in 3 axial and 3 stereo superlayers with at least 7 hits in each.

- $|z_0 - z_{\text{vtx}}|$:

  This variable is separation between z coordinate of the closest approach point with respect to run average beam line (z_0) and primary vertex z position (z_{vtx}).

- d_0(Impact parameter) :

  This variable ids recalculated to take the x coordinate of the primary vertex.

- Conversion removal :

  To remove conversion pair condidate, two variables is used. One variable is $\Delta(\cot\theta)$. This is simply the difference in $\cot\theta$ of the two tracks. another variable is separation δ_{xy}. This is found by first collapsing the helicies of two tracks into the two cicles on the $x-y$ plane.

$$|\Delta(\cot\theta)| < 0.04, \text{ and } |\delta_{xy}| < 0.2 \tag{3.3}$$

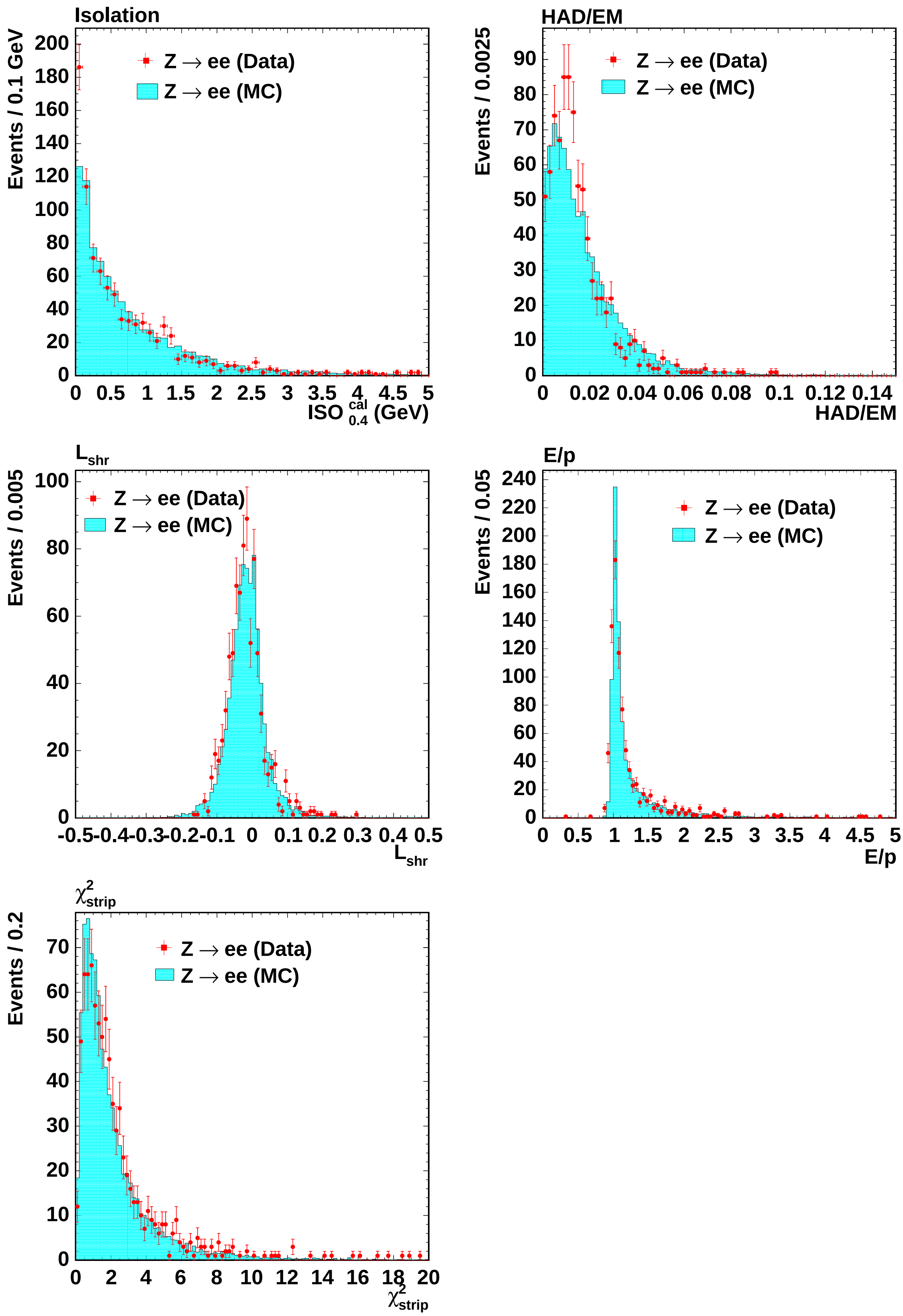

Figure 3.1: The electron variables used for the selection of events. The loose electron in the $Z \to e^+e^-$ candidates events. All the selection cut are applied each variable excluding the variable itself (Isolation, HAD/EM, L_{shr}, E/p and χ^2_{strip}).

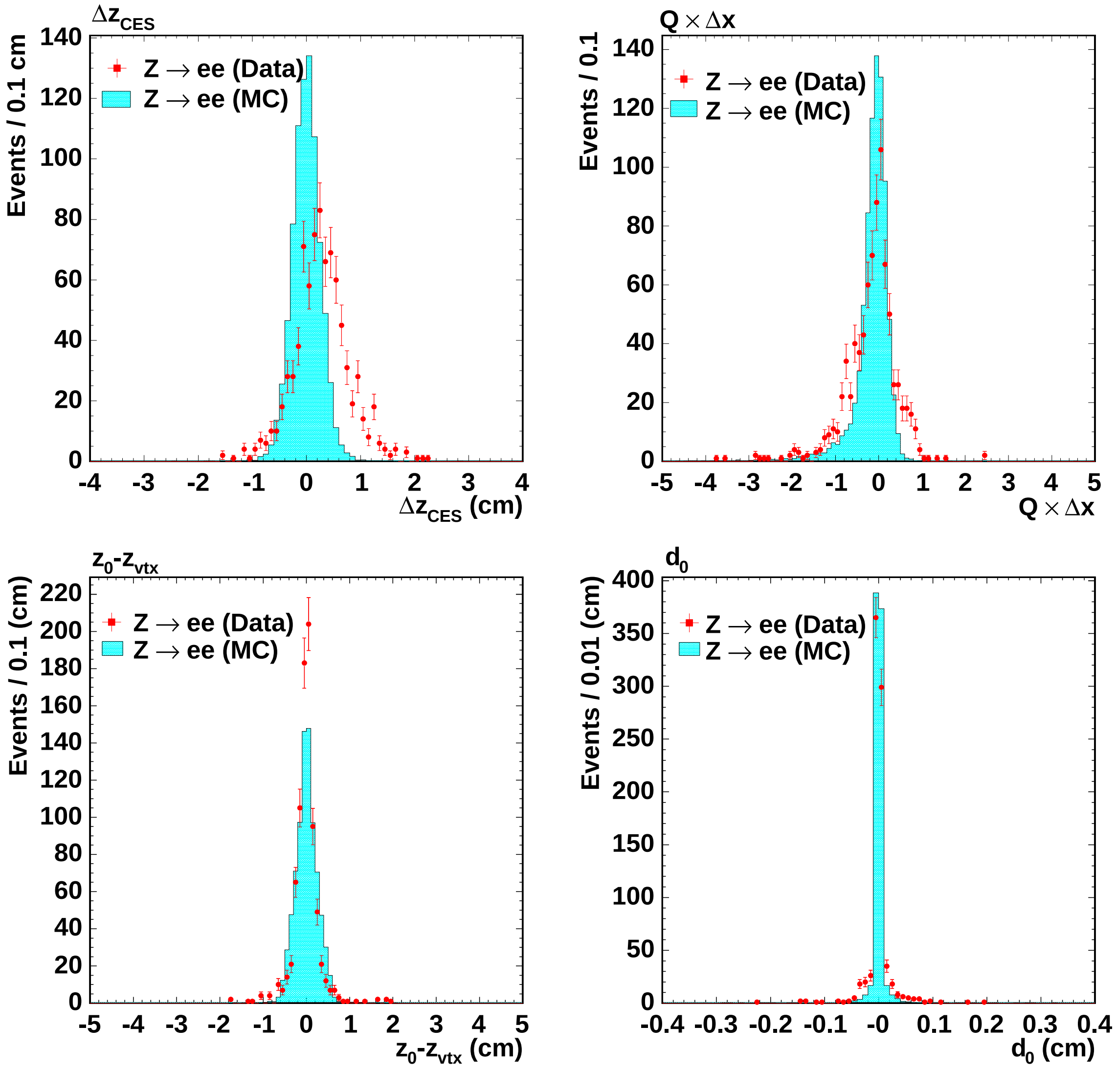

Figure 3.2: The electron variables used for the selection of events. The loose electron in the $Z \to e^+e^-$ candidates events. All the selection cut are applied each variable excluding the variable itself (Δz_{CES}, $Q \times \Delta x_{\text{CES}}$, $z_0 - z_{\text{vtx}}$ and d_0).

3.1.3 Muon Selection Variables

The variables are to select the central muons. The variable is the following.

- Fiduciality :

  For the CMUP and CMX muons, we require that the CMP or CMX stub satisfies thr following two requiremant:

  - In the direction of the drift wire, the track has to be extrapolated to be at least 3 cm insideof the chamber: fiducial z distance < -3 cm for CMUP amd CMX.
  - In the diraction perpendicular to the drift wire, the track has to be extrapolated to be inside of the chamber: fiducial x distance < 0 cm for CMP and CMX.

- COT exit radius ρ :

  CMX muons require that the COT exit radius ρ of the track. ρ is the following,

$$\rho = \frac{\eta}{|\eta|} \cdot \frac{z_{\mathrm{COT}} - z_0}{\tan(\frac{\pi}{2} - \theta)} \tag{3.4}$$

- p_T :

  The transverse momentum of the COT beam constrained track as measured using the track curvature in the COT.

- EM :

  Energy deposited to central electromagnetic calorimeter. However, Energy depsition increases as momentum increases. So to maintain good efficiency, EM must have sliding such as the following,

$$\mathrm{EM} = 2 + 0.0115(p - 100). \tag{3.5}$$

  This sliding is chosen to maintain 98% efficient.

- HAD :

  Energy deposited to central hadronic calorimeter. However, Energy depsition increases as momentum increases. So to maintain good efficiency, HAD must have sliding such as the following,

$$\mathrm{HAD} = 6 + 0.028(p - 100). \tag{3.6}$$

  This sliding is chosen to maintain 97% efficient.

- $r \times \Delta\phi$:

  This variable is Track and stub matching in the central muon chambers in $r - \phi$ plan.

- Track Quality :

  To ensure that the track associated with the electron is good quality reconstructed track, require that track hes been reconstructed in the COT in 3 axial and 3 stereo superlayers with at least 7 hits in each.

- $|z_0 - z_{\rm vtx}|$:

  This variable is separation between z coordinate of the closest approach point with respect to run average beam line (z_0) and primary vertex z position ($z_{\rm vtx}$).

- d_0(Impact parameter) :

  This variable is recalculated to take the x coordinate of the primary vertex.

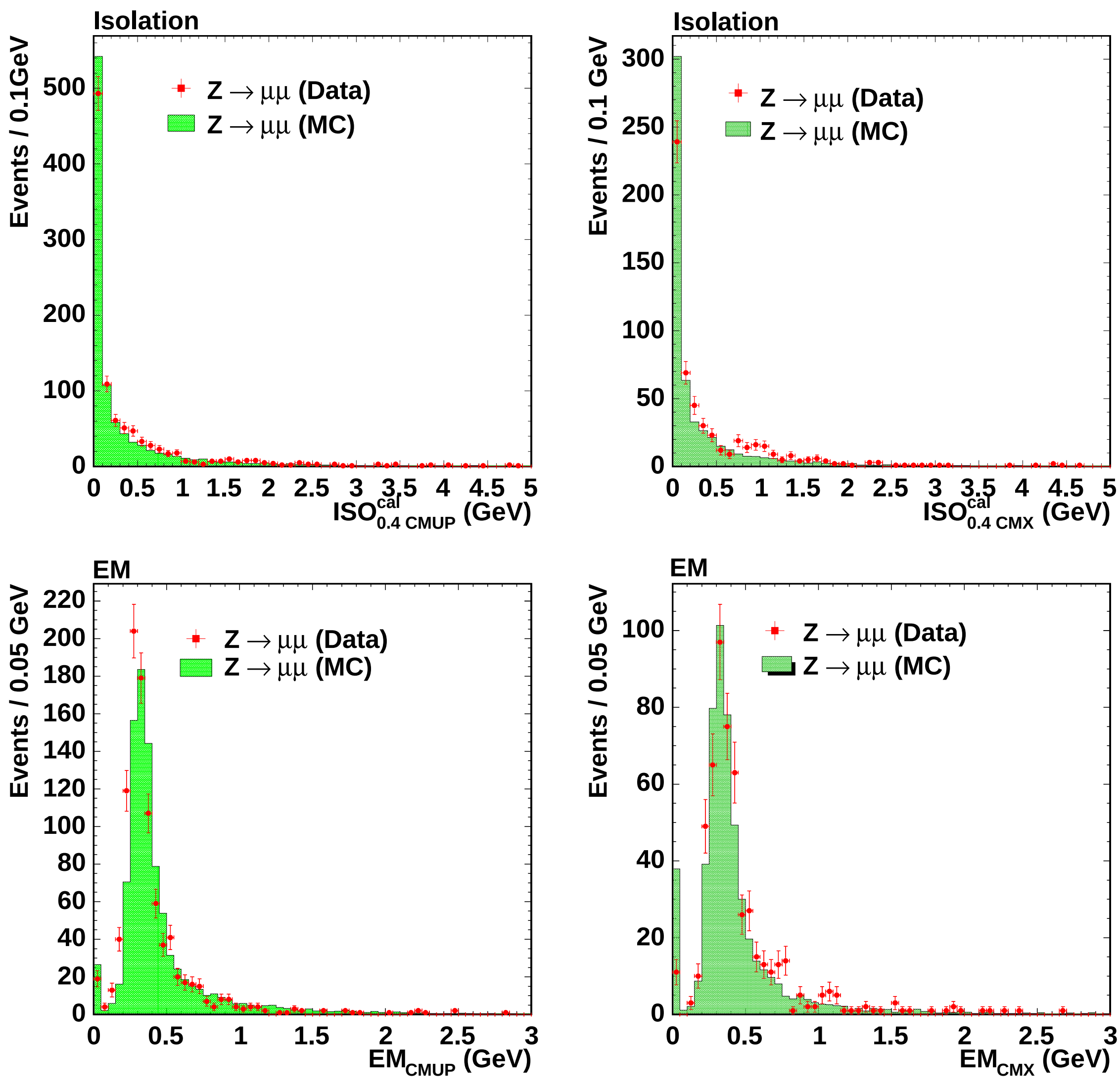

Figure 3.3: The muon variables used for the selection of events. The loose muon in the $Z \rightarrow \mu^+\mu^-$ candidates events. All the selection cut are applied each variable excluding the variable itself (Isolation, EM).

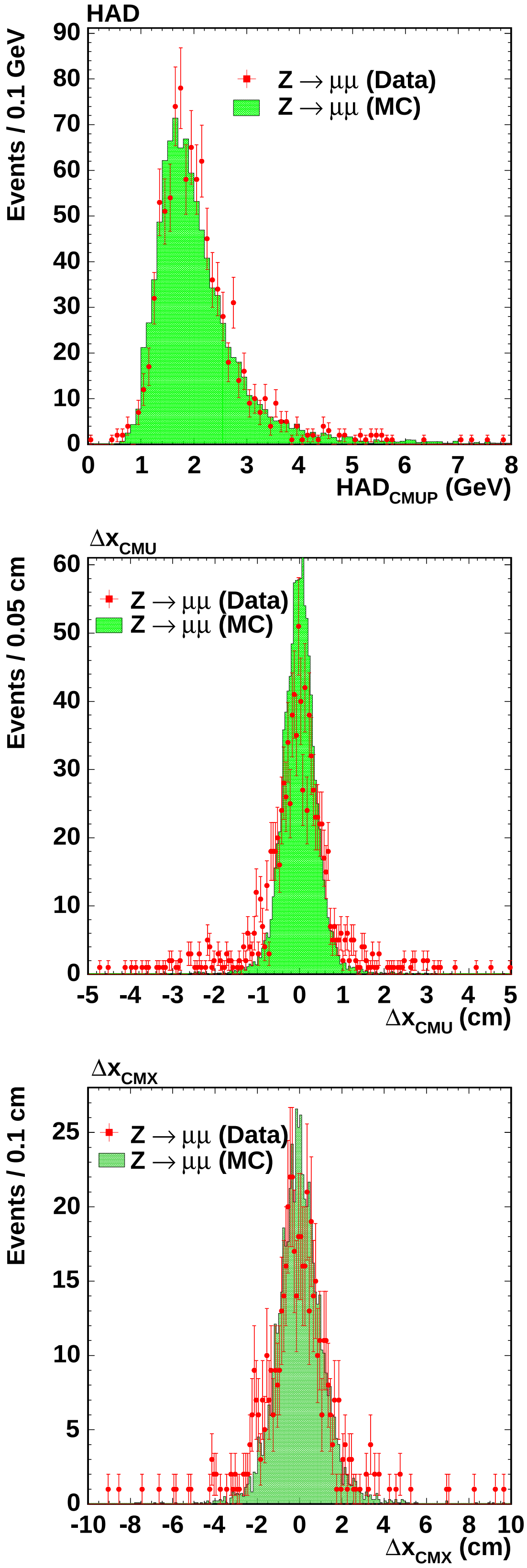

Figure 3.4: The muon variables used for the selection of events. The loose muon in the $Z \to \mu^+\mu^-$ candidates events. All the selection cut are applied each variable excluding the variable itself (HAD and $r \times \Delta\phi$).

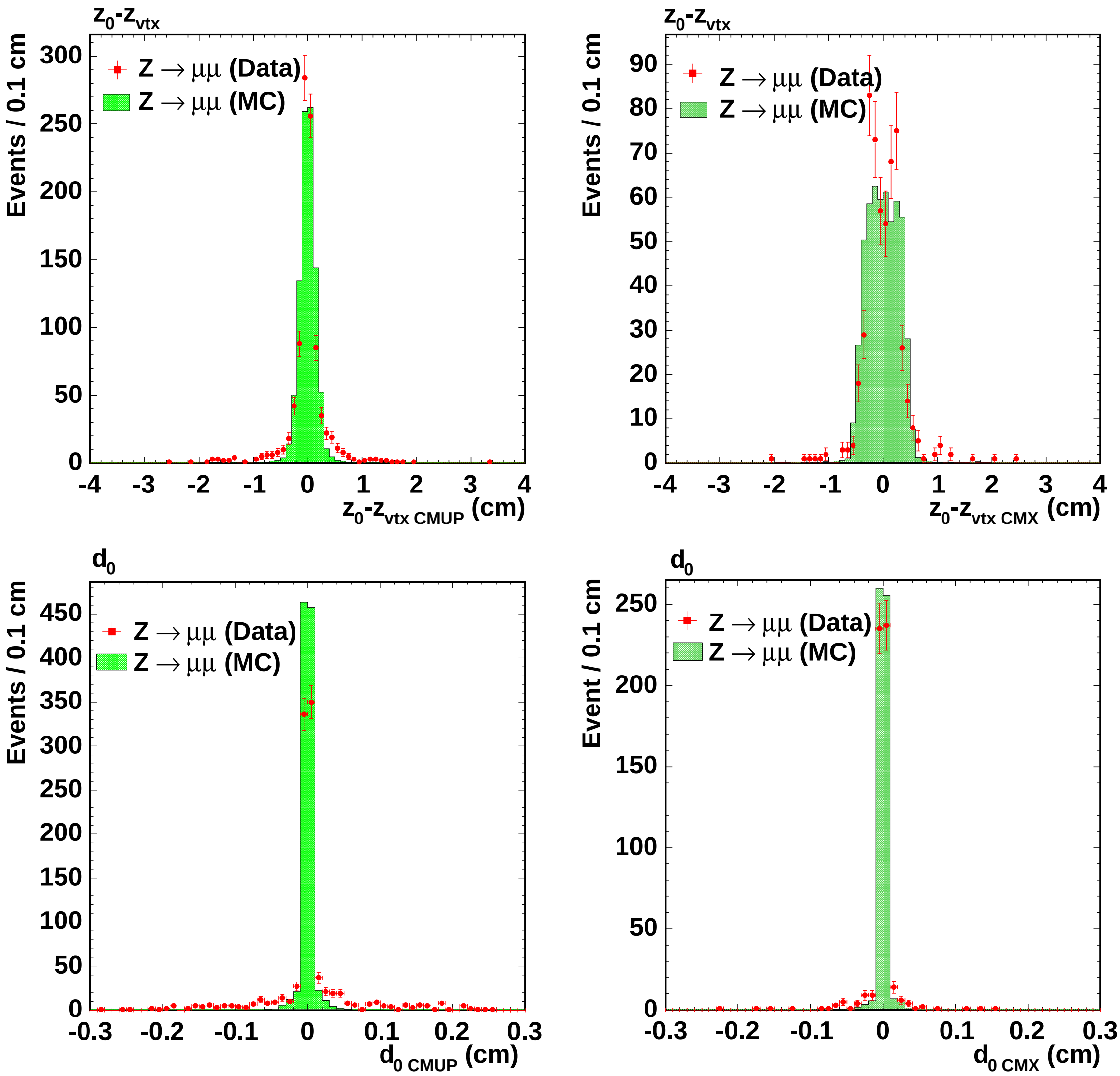

Figure 3.5: The muon variables used for the selection of events. The loose muon in the $Z \rightarrow \mu^+\mu^-$ candidates events. All the selection cut are applied each variable excluding the variable itself ($z_0 - z_{\mathrm{vtx}}$ and d_0).

Electron selection	Muon selection
Event vertex cut	
$\lvert z_{\mathrm{vtx}}\rvert < 60$ cm	
Geometrical and Kinematical cuts	
CEM	CMUP or CMX
Fiducial	Fiducial (CMUP), $\rho_{\mathrm{COT}} > 140$ cm (CMX)
$E_T^{\ell_1} > 20$ GeV ($p_T > 10$ GeV/c)	$p_T^{\ell_1} > 20$ GeV/c
$E_T^{\ell_2} > 6$ GeV ($p_T > 6$ GeV/c)	$p_T^{\ell_2} > 6$ GeV/c
Isolation cut	
$\mathrm{ISO}_{0.4}^{\mathrm{cal}} < 2$ GeV	
Identification cuts	
HAD/EM $< 0.055 + 0.00045 \times E$	EM $<$ max(2, 2+0.0115$\times$(p $-$ 100)) GeV
$L_{\mathrm{shr}} < 0.2$ ($E_T < 70$ GeV)	HAD $<$ max(6, 6+0.0280$\times$(p $-$ 100)) GeV
$E/p < 2$ ($E_T < 50$ GeV)	$\lvert r \times \Delta\phi\rvert < 3, 5, 6$ cm (CMU, P, X)
$\chi^2_{\mathrm{strip}} < 10$	
$\lvert\Delta z_{\mathrm{CES}}\rvert < 3$ cm	
$-3.0 < Q \times \Delta x_{\mathrm{CES}} < 1.5$ cm	
Track quality: stereo ≥ 3 and axial ≥ 3, ≥ 7 hits	
$\lvert z_0 - z_{\mathrm{vtx}}\rvert < 2$ cm	
$\lvert d_0\rvert < 0.2$ cm (silicon hits < 3), 0.02 cm (≥ 3)	
Conversion removal	

Table 3.1: Primary vertex and lepton selection cuts

3.2 Selection Cut Efficiency

The talal detection efficiency in this analysis can be written as

$$\varepsilon_{\mathrm{tot}} = A \cdot \varepsilon_{\mathrm{Iso}} \cdot \varepsilon_{\mathrm{ID}} \cdot \varepsilon_{\mathrm{rec}} \cdot \varepsilon_{\mathrm{trig}}, \tag{3.7}$$

where A is geometrical and kinematical acceptance, $\varepsilon_{\mathrm{Iso}}$ is isolation cut efficiency, $\varepsilon_{\mathrm{ID}}$ is identification cut efficiency, $\varepsilon_{\mathrm{rec}}$ is muon reconstruction efficiency and $\varepsilon_{\mathrm{trig}}$ is trigger efficiency. A is estimated using MC. $\varepsilon_{\mathrm{Iso}}$, $\varepsilon_{\mathrm{ID}}$ and $\varepsilon_{\mathrm{rec}}$ are estimated using data and MC, furthermore from these data and MC efficiency, we estimate Scale Factor. $\varepsilon_{\mathrm{trig}}$ is not estiemted on this analysis, qoted CDF note 6234 [14] for Electron trigger efficiency and CDF note 7031 [15] for Muon trigger efficiency.

3.2.1 Geometrical and Kinematical Acceptance

We estimate the geometrical and kinematical acceptance using MC sample. We match the OBSP level lepton from decaying Z with the CDF level lepton using $dR = \sqrt{d\phi^2 + d\eta^2}$, where $d\phi = \phi_{\mathrm{OBSP}} - \phi_{\mathrm{CDF}}$, $d\eta = \eta_{\mathrm{OBSP}} - \eta_{\mathrm{CDF}}$. In the OBSP lepton, the momentum and energy of gamma, which emitted from OBSP, is subtracted, then calculate ϕ_{OBSP} and η_{OBSP} using subtracted OBSP lepton. In the CDF lepton, we select the lepton not applying selection cut, which pair with a lepton passing tight selection cut. dR cut value is that for electron $dR < 0.04$, for muon $dR < 0.02$. We apply the geometrical and kinematical cut to the matched CDF lepton and estimate the acceptance by the following simple fraction

$$A = \frac{\text{The number of Matched CDF leptons after cut}}{\text{The number of Matched CDF leptons befre cut}} \tag{3.8}$$

Therefore, We estimate ratio of HEPG level remianing events after cut to CDF level remaning events after cut. This mean is likely mapping (f : HEPG $\rightarrow$ CDF). Table 3.2 shows the Acceptance with $p_T > 6$ GeV/c leptons on the HEPG and CDF level. Table 3.3 shows the ratios of remaining events after each cuts for HEPG to CDF level. Figure 3.6 shows the matched lepton dR distributions, the red lines are dR cut values.

	HEPG		
Type	Geom	Kine	Geom & Kine
CEM-CEM	0.518±0.002	0.9998±0.0002	0.518±0.001
CMUP-CMUP	0.287±0.002	0.9999±0.0001	0.287±0.002
CMX-CMUP	0.298±0.002	0.9999±0.0001	0.298±0.002
CMX-CMX	0.181±0.002	0.9997±0.0002	0.181±0.002
CMUP-CMX	0.184±0.002	0.9998±0.0001	0.184±0.002
	CDF		
Type	Geom	Kine	Geom & Kine
CEM-CEM	0.572±0.003	0.907±0.002	0.520±0.003
CMUP-CMUP	0.247±0.002	0.9994±0.0003	0.246±0.002
CMX-CMUP	0.245±0.003	0.9984±0.0007	0.245±0.004
CMX-CMX	0.128±0.003	0.9995±0.0005	0.128±0.003
CMUP-CMX	0.115±0.002	0.9984±0.0007	0.115±0.002

Table 3.2: The geomatriacal and kinematical Acceptance with $p_T > 6$ GeV/c lepton on the HEPG and CDF level.

Type	No cut	Geom	Geom & Kine
CEM-CEM	0.545±0.002	0.603±0.003	0.547±0.003
CMUP-CMUP	0.491±0.002	0.422±0.004	0.421±0.004
CMX-CMUP	0.372±0.002	0.306±0.004	0.306±0.004
CMX-CMX	0.372±0.002	0.262±0.005	0.262±0.005
CMUP-CMX	0.491±0.002	0.307±0.004	0.306±0.004

Table 3.3: The ratio of remaning events after the geometrical to kinematical cut. The Ratio = CDF/HEPG.

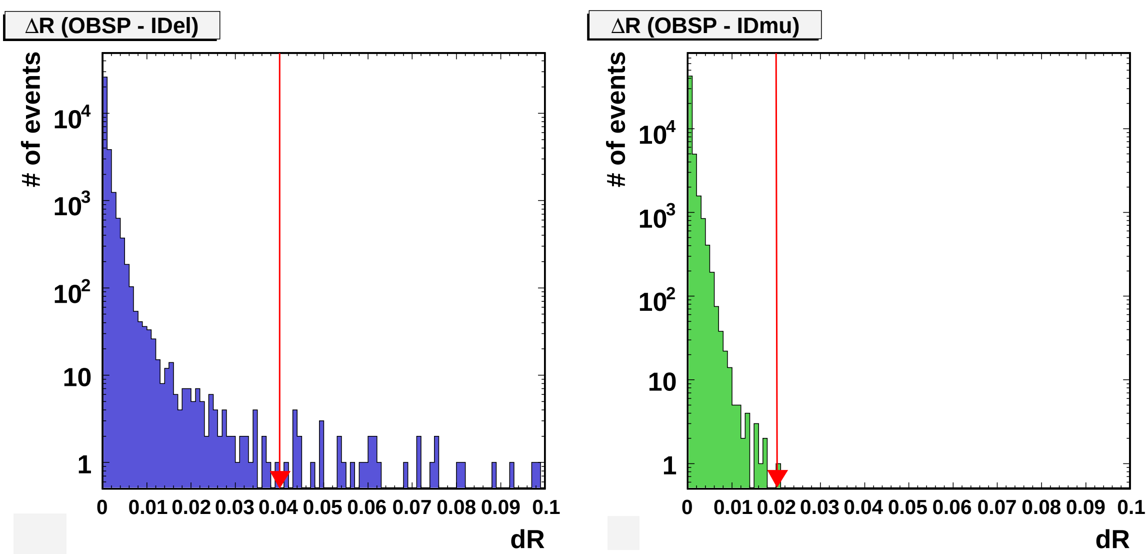

Figure 3.6: The matched lepton dR distributions (left: electron, right: muon). The red lines are dR cut values.

3.2.2 Isolation Cut Efficiency

We estimate Isolation cut efficiency using Data and MC, moreover from Data and MC efficency, estimate Scale Factor (Data/MC). Explain method of efficiency estimation. In first, pick up an opposite sign lepton pair, because we estimate the efficiency using $Z \to \ell\ell$ events. Next, we apply the geometrical, kinematical, isolation and identification cut (namely, apply all selection cuts) to the one leg of $Z \to \ell\ell$, where the kinematical cut is E_T and/or $p_T > 20.0$ GeV, the passing lepton is called "1st leg lepton". For the remaining event, which the 1st leg passing all selection cuts, we apply the geometrical and kinematical cuts to other leg, where the kinematical cut is E_T and/or $p_T > 6.0$ GeV, the other passing leg is called "2nd leg lepton". Then, we reconstruct Z mass, which is invariant mass, and count the number of Z events by integrate the gaussian part of fitting function (3.10), which fit to Z mass distribution,

$$M_Z = \sqrt{(E_+ + E_-)^2 - (p_+ + p_-)^2}, \tag{3.9}$$

$$f_{Fit}(x) = Ae^{-\frac{(x-\mu)^2}{2\sigma^2}} + Bx + C \ (x\text{: mass}). \tag{3.10}$$

Next, we apply the isolation cut to the 2nd lepton and for remaining events, again reconstruct and count Z events in the same procedure as above. Finally, we calculate the efficiency by the simple fraction:

$$\varepsilon_{\text{Iso}} = \frac{\text{The number of } Z \text{ events after cut}}{\text{The number of } Z \text{ events before cut}}. \tag{3.11}$$

As the same time, we compare this result with previous result [16] by looking at Data ratio

$$\text{Data ratio} = \frac{\text{This data efficiency}}{\text{Previous data efficiency}} \tag{3.12}$$

We saw the difference in efficiency, particularly in CEM. This difference have two reasons. The first reason is by cut method. For previous analysis, pick up same or oppsite sign lepton pair and these leptons are both passing tight cut (E_T and/or $p_T > 20.0$ GeV). The second reason is by offline release version. This analysis use `5.3.3`, while previous analysis have used `4.11.1`. Table 3.5 shows the difference in the efficiency on account of cut methods and offline release versions.

Type	CDF7262			This analysis		
	Data($Z\to ee$)	MC($Z\to ee$)	Scale Factor	Data($Z\to ee$)	MC($Z\to ee$)	Scale Factor
CEM	0.823 ± 0.006	0.833 ± 0.002	0.988 ± 0.007	0.921 ± 0.009	0.895 ± 0.003	1.029 ± 0.011
CMUP	0.916 ± 0.007	0.937 ± 0.002	0.978 ± 0.008	0.936 ± 0.010	0.954 ± 0.003	0.981 ± 0.011
CMX	0.929 ± 0.007	0.930 ± 0.002	0.999 ± 0.008	0.959 ± 0.010	0.963 ± 0.003	0.996 ± 0.011

Table 3.4: Isolation cut efficiency for $Z \to \ell\ell$ Data and MC, also show previous result.

	Previous Method	This Method
`4.11.1`	0.833 ± 0.002	0.846 ± 0.002
`5.3.3`	0.857 ± 0.004	0.895 ± 0.003

Table 3.5: The difference in the efficiency on account of cut methods and offline release versions using MC.

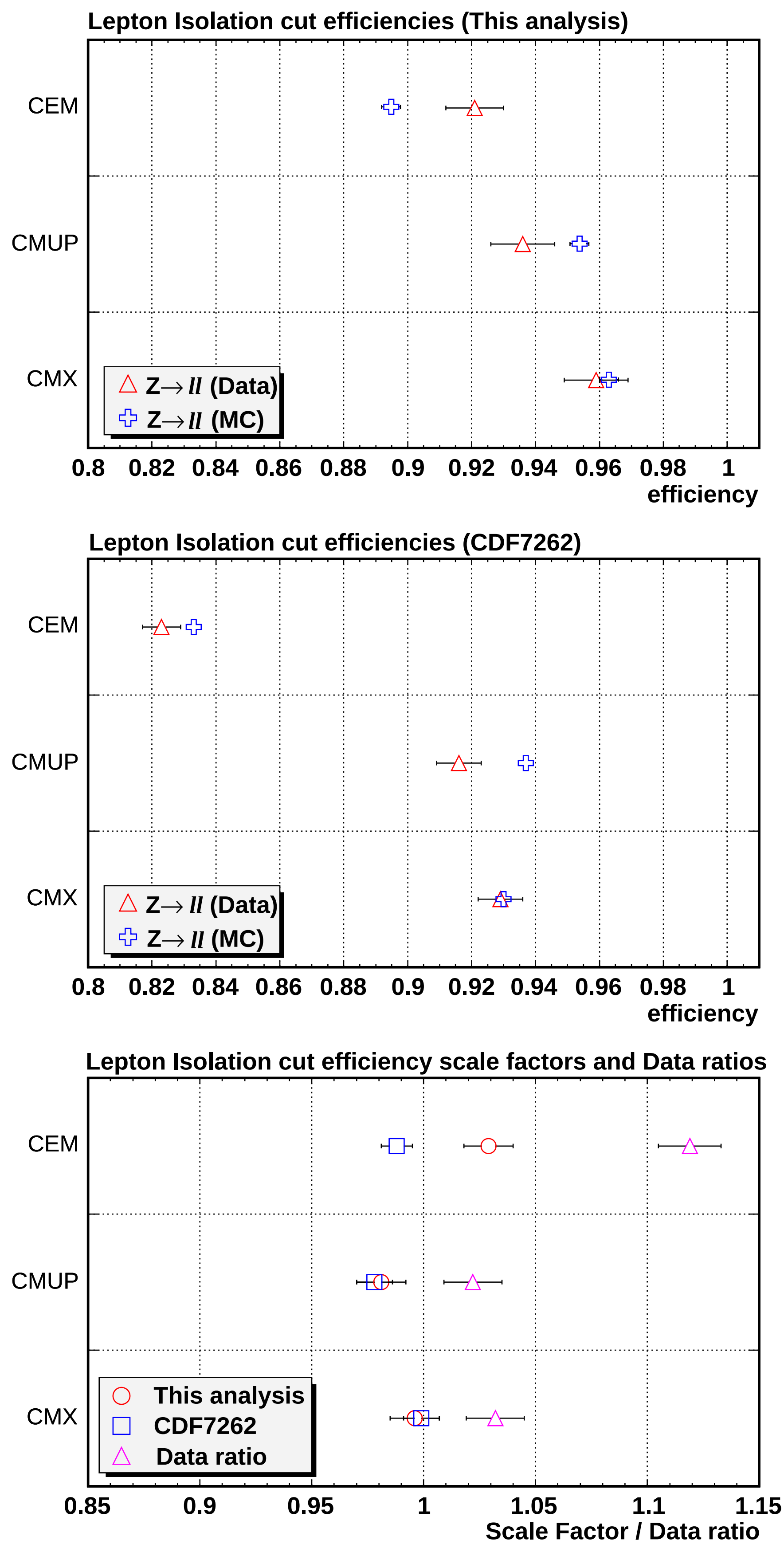

Figure 3.7: Isolation cut efficiency. From upper to lower: This analysis, Previous analysis and Scale Factor and Data ratio.

3.2.3 Identification Cut Efficiency

We also estimate the idendification cut efficiency and sacle factor. The estimation is basically same as isolation cut estimation excluding the cut appling to the 2nd leg lepton. For identification cut efficiency, we first apply geometrical, kinematical and isolation cut to 2nd leg. Then, as same as the isolation cut efficiency estimaion, reconstruct the mass and count Z events by function fitting. Next, apply identification cut to 2nd leg and reconstruct and count Z event. Finally, we calculate efficiency by the simple fraction.

We also compare this result with previous result. We saw the several diiferences in identification cut efficiencies. At the first, for electron identification cut, we saw the differences in E/p or χ^2_{strip}. The reason for E/p is our using offline version [17] (This analysis: `5.3.3`, Previous analysis: `4.11.1`). The reason for χ^2_{strip} is the difference of its definition, our cut variable has the scaling function which to correct χ^2_{strip} for energy dependence, while previous variable does not have it (The scaling function: $0.1792 \times 2.11^{\log E}$). For muon identification, we saw the difference in $r \times \Delta\phi$ particular CMUP-CMUP and CMX-CMUP. The reason is the difference in cut method, our method is that apply Δx_{CMU} and Δx_{CMP}, whlie previous is Δx_{CMU} or Δx_{CMP}.

Cut Variable	Data($Z \to ee$)	MC($Z \to ee$)	Scale Factor	Data($Z \to ee$)	MC($Z \to ee$)	Scale Factor
	CDF7262			This analysis		
HAD/EM	0.993±0.001	0.989±0.001	1.000±0.001	0.992±0.003	0.989±0.001	1.003±0.003
L_{shr}	0.991±0.001	0.974±0.001	1.020±0.001	0.996±0.002	0.992±0.001	1.004±0.002
E/p	0.932±0.003	0.939±0.001	0.993±0.003	0.910±0.010	0.900±0.003	1.011±0.012
χ^2_{strip}	0.993±0.001	0.998±0.001	0.995±0.001	0.962±0.007	0.979±0.001	0.983±0.007
$\|\Delta z_{\mathrm{CES}}\|$	0.994±0.001	0.996±0.001	0.997±0.001	0.999±0.001	0.998±0.001	1.001±0.001
$Q \times \Delta x_{\mathrm{CES}}$	0.980±0.002	0.991±0.001	0.989±0.002	0.985±0.004	0.982±0.001	1.003±0.004
Track quality	0.974±0.002	0.992±0.001	0.982±0.002	0.961±0.007	0.994±0.001	0.967±0.007
$\|z_0 - z_{\mathrm{vtx}}\|$	0.986±0.001	0.992±0.001	0.994±0.001	0.999±0.001	0.995±0.001	1.004±0.001
$\|d_0\|$	0.971±0.002	0.984±0.001	0.986±0.002	0.986±0.004	0.979±0.001	1.007±0.004
Conversion veto	0.943±0.003	0.967±0.001	0.976±0.003	0.950±0.008	0.947±0.002	1.003±0.009
Total	0.822±0.005	0.862±0.001	0.954±0.006	0.784±0.015	0.811±0.004	0.967±0.019

Table 3.6: Electron identification cut efficiency for $Z \to ee$ Data and MC.

	CMUP-CMUP					
Cut Variable	Data($Z \to \mu\mu$)	MC($Z \to \mu\mu$)	Scale Factor	Data($Z \to \mu\mu$)	MC($Z \to \mu\mu$)	Scale Factor
	CDF7262			This analysis		
EM	0.968±0.004	0.959±0.001	1.000±0.000	0.985±0.007	0.970±0.003	1.015±0.008
HAD	0.981±0.003	0.977±0.001	1.010±0.000	0.979±0.008	0.978±0.002	1.001±0.008
$r \times \Delta\phi$	0.998±0.001	0.999±0.001	1.000±0.000	0.957±0.011	0.996±0.001	0.961±0.011
Track Quality	0.977±0.003	0.996±0.001	0.982±0.003	0.986±0.006	0.998±0.001	0.988±0.006
$\lvert z_0 - z_{\rm vtx}\rvert$	0.995±0.002	0.998±0.001	0.997±0.002	0.992±0.005	0.999±0.001	0.993±0.005
$\lvert d_0\rvert$	0.996±0.001	0.998±0.001	0.998±0.001	0.999±0.001	0.998±0.001	1.001±0.001
Total	0.923±0.006	0.930±0.001	0.993±0.007	0.901±0.016	0.944±0.004	0.954±0.017

	CMX-CMUP					
Cut Variable	Data($Z \to \mu\mu$)	MC($Z \to \mu\mu$)	Scale Factor	Data($Z \to \mu\mu$)	MC($Z \to \mu\mu$)	Scale Factor
	CDF7262			This analysis		
EM	0.944±0.010	0.930±0.002	1.020±0.010	0.963±0.012	0.976±0.004	0.987±0.013
HAD	0.979±0.006	0.955±0.002	1.020±0.010	0.991±0.006	0.987±0.003	1.004±0.007
$r \times \Delta\phi$	0.996±0.003	0.999±0.001	0.997±0.003	0.926±0.017	0.994±0.002	0.932±0.017
Track Quality	0.958±0.009	0.994±0.001	0.965±0.009	0.983±0.008	0.996±0.002	0.987±0.008
$\lvert z_0 - z_{\rm vtx}\rvert$	0.983±0.006	0.995±0.001	0.988±0.006	0.997±0.004	0.998±0.001	0.999±0.004
$\lvert d_0\rvert$	0.993±0.004	0.996±0.001	0.997±0.004	0.999±0.001	0.999±0.001	1.000±0.001
Total	0.868±0.015	0.873±0.003	0.993±0.017	0.880±0.021	0.949±0.005	0.927±0.023

	CMX-CMX					
Cut Variable	Data($Z \to \mu\mu$)	MC($Z \to \mu\mu$)	Scale Factor	Data($Z \to \mu\mu$)	MC($Z \to \mu\mu$)	Scale Factor
	CDF7262			This analysis		
EM	0.954±0.009	0.962±0.002	0.992±0.009	0.944±0.019	0.967±0.006	0.976±0.021
HAD	0.983±0.005	0.970±0.001	1.010±0.001	0.979±0.012	0.989±0.004	0.990±0.013
$r \times \Delta\phi$	0.974±0.007	0.998±0.001	0.976±0.007	0.986±0.010	0.999±0.001	0.987±0.010
Track Quality	0.977±0.006	0.993±0.001	0.984±0.006	0.968±0.014	0.999±0.001	0.969±0.014
$\lvert z_0 - z_{\rm vtx}\rvert$	0.991±0.004	0.998±0.001	0.993±0.004	0.976±0.013	0.999±0.001	0.970±0.013
$\lvert d_0\rvert$	0.995±0.003	0.998±0.001	0.997±0.003	0.989±0.008	0.999±0.001	0.990±0.008
Total	0.884±0.013	0.922±0.002	0.960±0.015	0.839±0.030	0.954±0.007	0.879±0.032

	CMUP-CMX					
Cut Variable	Data($Z \to \mu\mu$)	MC($Z \to \mu\mu$)	Scale Factor	Data($Z \to \mu\mu$)	MC($Z \to \mu\mu$)	Scale Factor
	CDF7262			This analysis		
EM	0.961±0.008	0.927±0.002	1.040±0.010	0.959±0.013	0.969±0.004	0.990±0.014
HAD	0.967±0.008	0.937±0.002	1.030±0.010	0.974±0.010	0.979±0.004	0.995±0.011
$r \times \Delta\phi$	0.954±0.009	0.995±0.001	0.959±0.009	0.975±0.010	0.999±0.001	0.976±0.010
Track Quality	0.971±0.007	0.987±0.001	0.984±0.007	0.980±0.009	0.998±0.001	0.982±0.009
$\lvert z_0 - z_{\rm vtx}\rvert$	0.987±0.005	0.995±0.001	0.992±0.005	0.999±0.001	0.999±0.001	1.000±0.001
$\lvert d_0\rvert$	0.986±0.005	0.998±0.001	0.989±0.005	0.999±0.001	0.999±0.001	1.000±0.001
Total	0.838±0.016	0.846±0.003	0.991±0.019	0.884±0.021	0.947±0.006	0.933±0.023

Table 3.7: Muon identification cut efficiency for $Z \to \mu\mu$ Data and MC. From upper to lower: CMUP-CMUP, CMX-CMUP, CMX-CMX, CMUP-CMX.

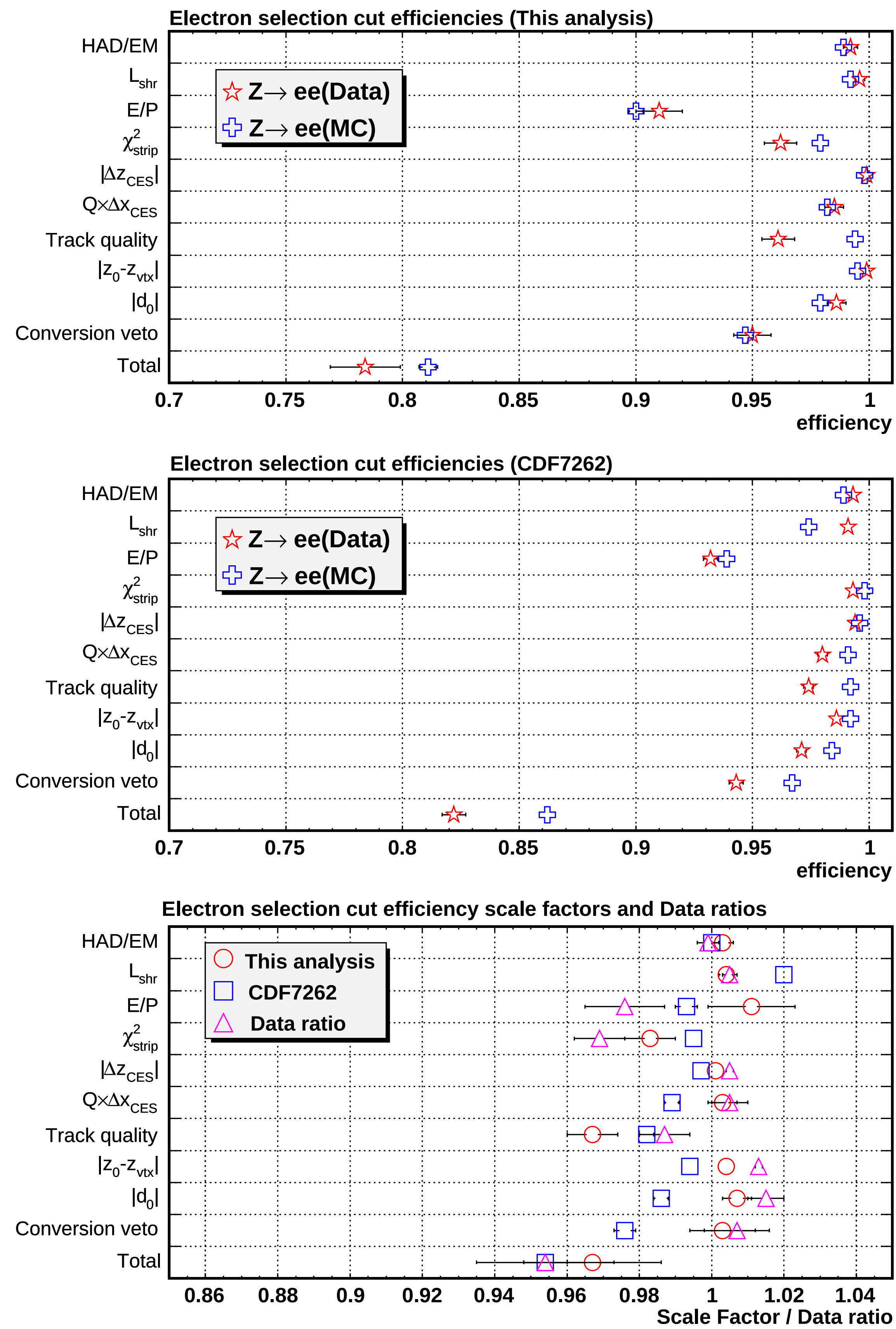

Figure 3.8: Electron identification cut efficiency. From upper to lower: This analysis, Previous analysis and Scale Factor and Data ratio.

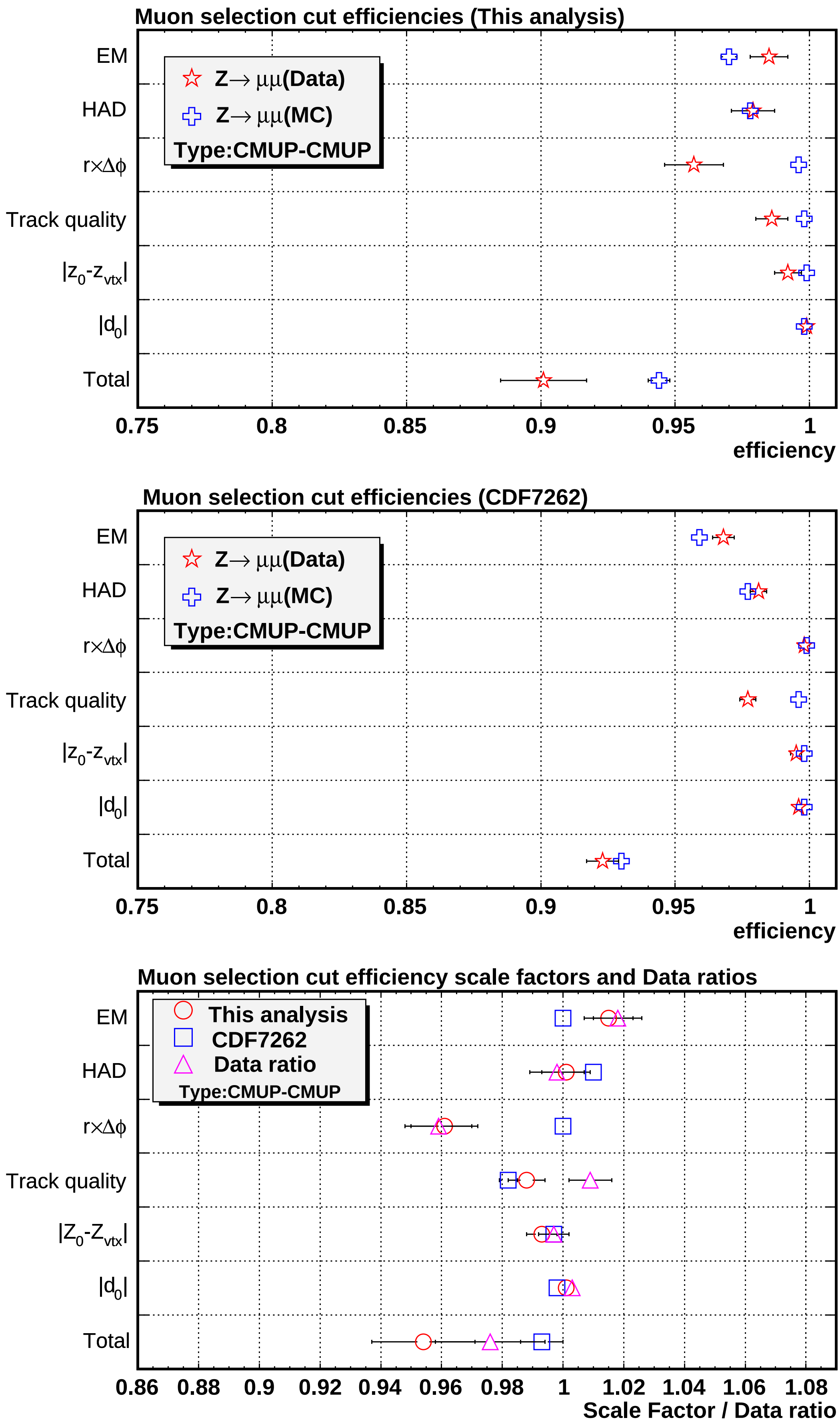

Figure 3.9: Muon identification cut efficiency (CMUP-CMUP). From upper to lower: This analysis, Previous analysis and Scale Factor and Data ratio.

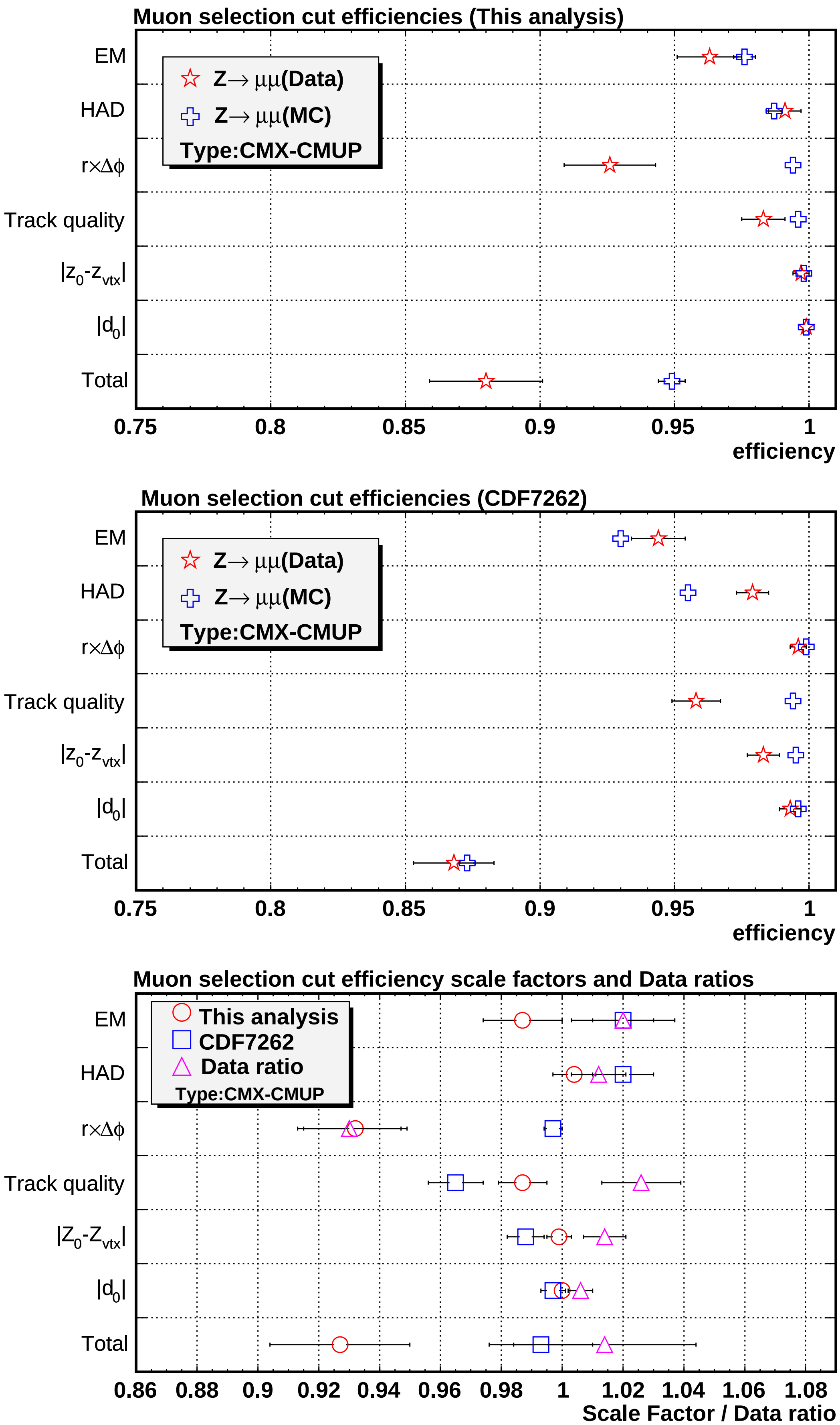

Figure 3.10: Muon identification cut efficiency (CMX-CMUP). From upper to lower: This analysis, Previous analysis and Scale Factor and Data ratio.

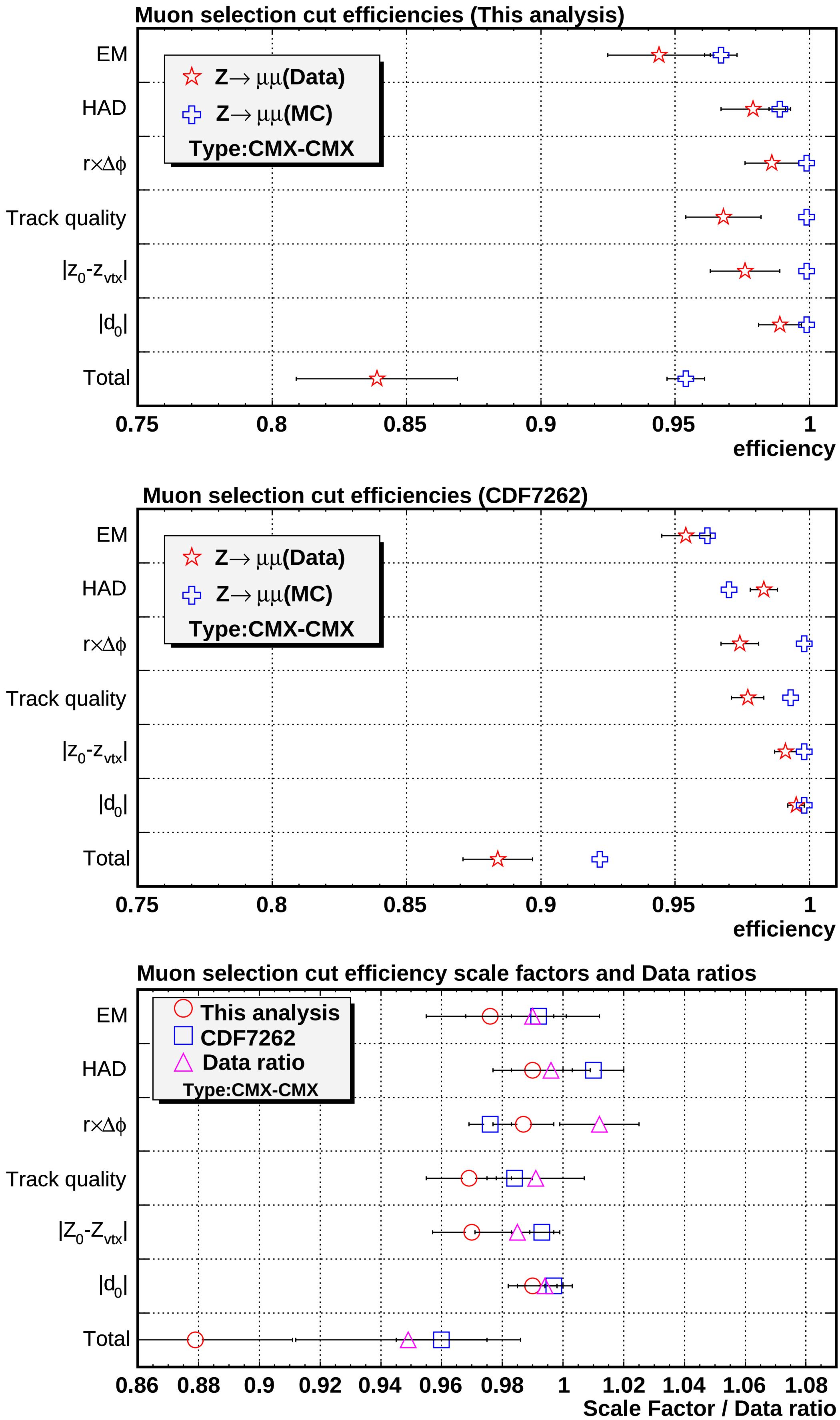

Figure 3.11: Muon identification cut efficiency (CMX-CMX). From upper to lower: This analysis, Previous analysis and Scale Factor and Data ratio.

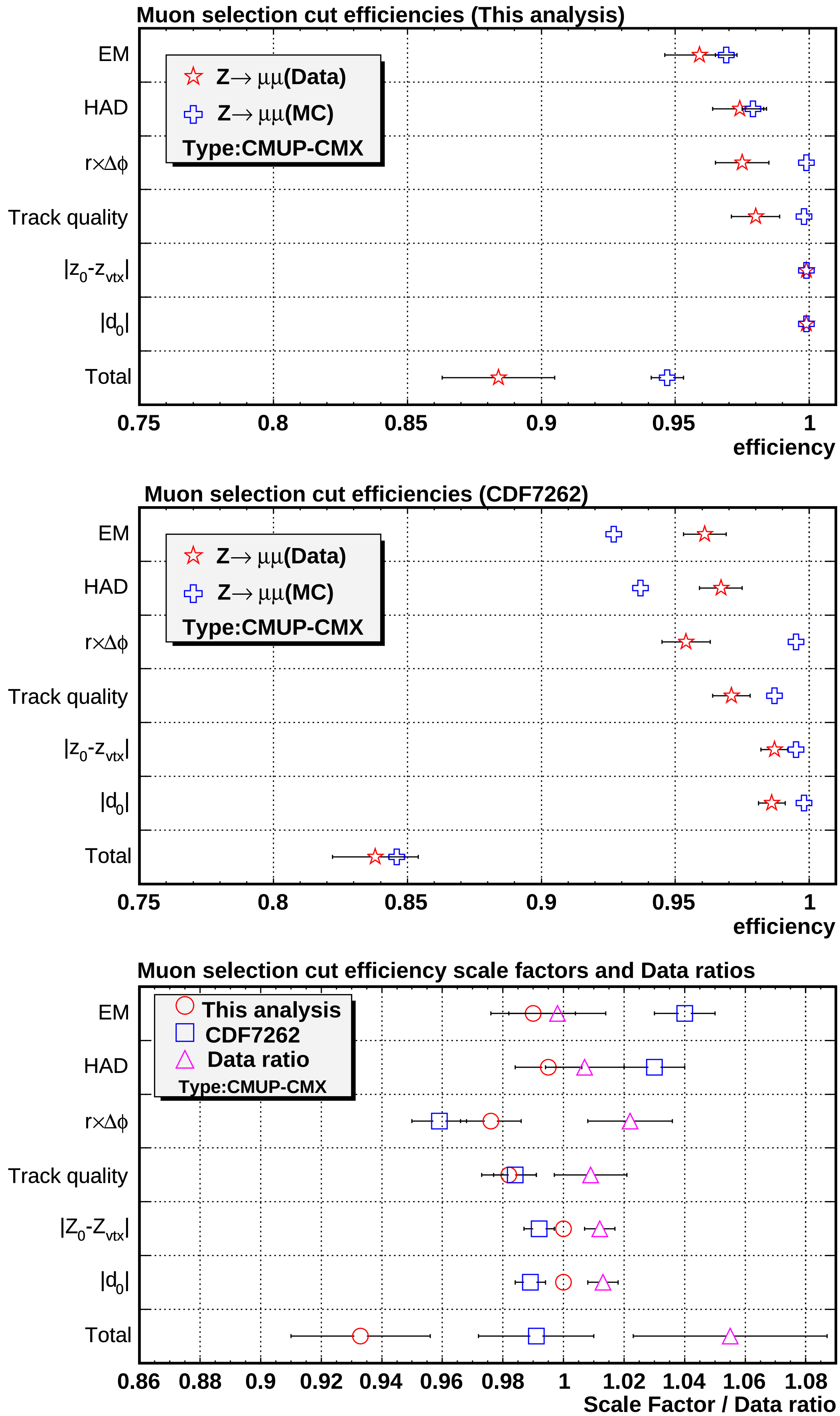

Figure 3.12: Muon identification cut efficiency (CMUP-CMX). From upper to lower: This analysis, Previous analysis and Scale Factor and Data ratio.

3.3 Reconstruction Efficiency and Sacle Factor for Muon chamber

We estimate the reconstruction efficiecncy for the muon chamber. This efficicency is mean that when a muon has η from COT tracking information, the muon has stub of same tracking η region or not. To estimate efficiency, we first pick up 1st leg muon passing all selection cut, and select the 2nd leg muon within Z mass window (81∼101 GeV/c^2) with the 1st leg muon. Then we look at η of the 2nd leg, moreover confirm that the 2nd muon have stub or not. We can get efficiecncy from in the following fraction:

$$\varepsilon_{\mathrm{rec}} = \frac{\text{Tne number of 2nd leg muon which have stub}}{\text{The number of 2nd leg muon which have tracking } \eta \text{ within stub } \eta \text{ region}}. \tag{3.13}$$

We saw that CMUP efficiency of MC is lower than Data efficiency, while CMX efficiency of MC is higher by estimating scale factor. However, we note that our using sample data is the difference in Run range for Data and MC (Data: 150287∼152954 and 175087∼179056, MC: 141572∼144424). Table 3.8 shows the reconstruction efficiency and scale factor. Figure 3.13 (Figure 3.14) shows η distributions of 2nd leg muon and efficiency each 0.1 η for 1st leg muon CMUP (CMX).

	Data	MC	Scale Factor
CMUP-CMUP	0.632±0.018	0.656±0.005	0.962±0.028
CMX-CMUP	0.603±0.024	0.633±0.007	0.953±0.039
CMUP-CMX	0.732±0.025	0.615±0.009	1.190±0.044
CMX-CMX	0.690±0.022	0.540±0.006	1.279±0.043

Table 3.8: Reconstuction efficiency and Scale Factor.

3.4 Trigger Efficiency

We referred to the trigger efficicency of `ELECTRON_CENTRAL_18` in [14] and that of `MUON_CMUP18` and `MUON_CMX18` in [15]. We note that these efficiency are estimated for E_T (p_T)> 20 GeV electron (muon). For our analysis, we have to estimate the trigger efficiency for E_T (p_T)> 6.0 GeV electron (muon), because the 2nd leg electron (muon) is required E_T (p_T)> 6.0 GeV. Table 3.9 shows the trigger efficiency for the electron and muon trigger.

	Trigger Efficiency
`ELECTRON_CENTRAL_18`	0.961±0.005
`MUON_CMUP18`	0.908±0.005
`MUON_CMX18`	0.965±0.004

Table 3.9: Trigger efficiency which is refferred to [14] and [15]

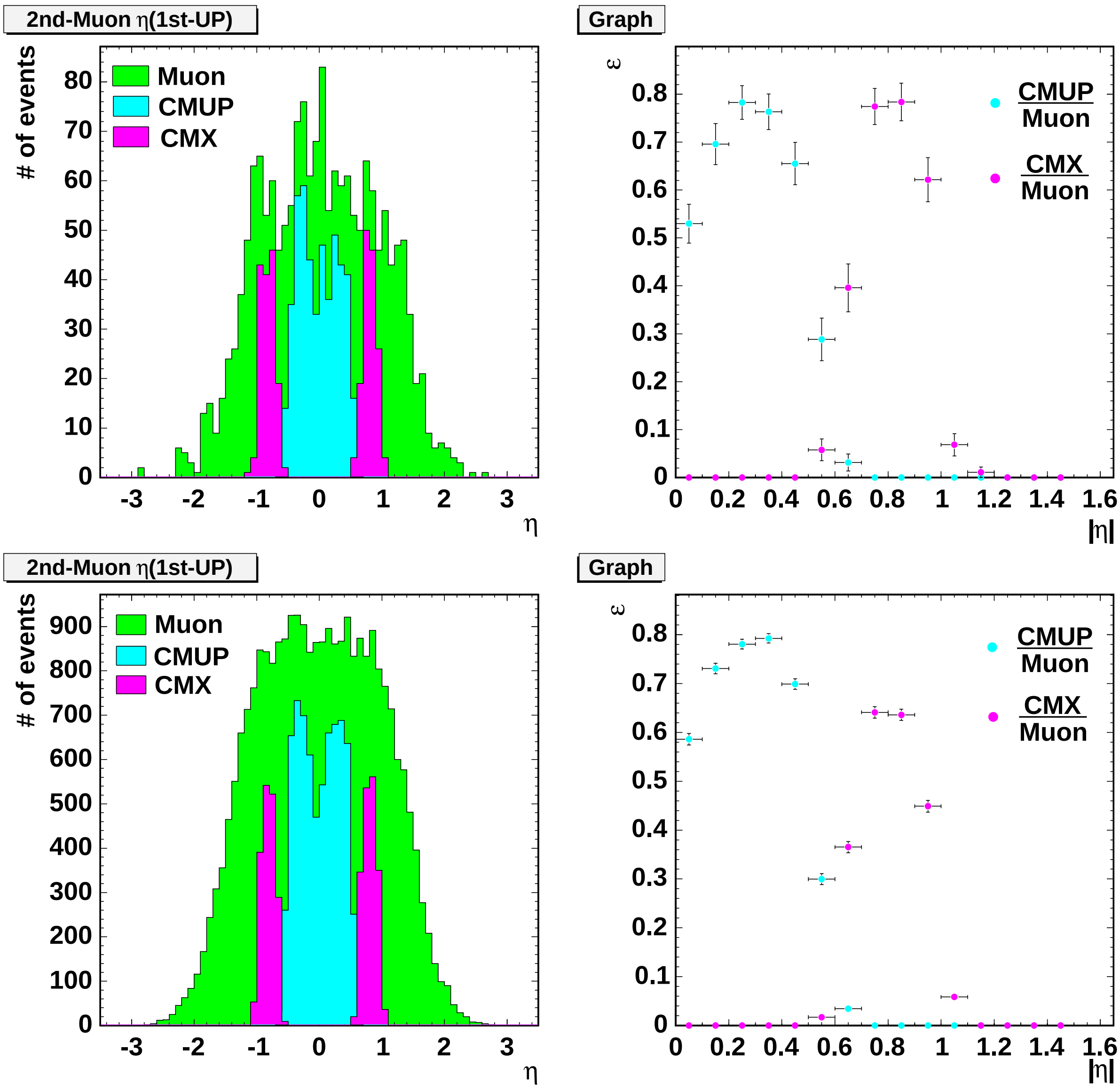

Figure 3.13: The η distribution (left figure) and Reconstrction efficiency each 0.1 η (right one). for the 1st muon CMUP. The upper two figures are from Data sample, the lower two figures are MC.

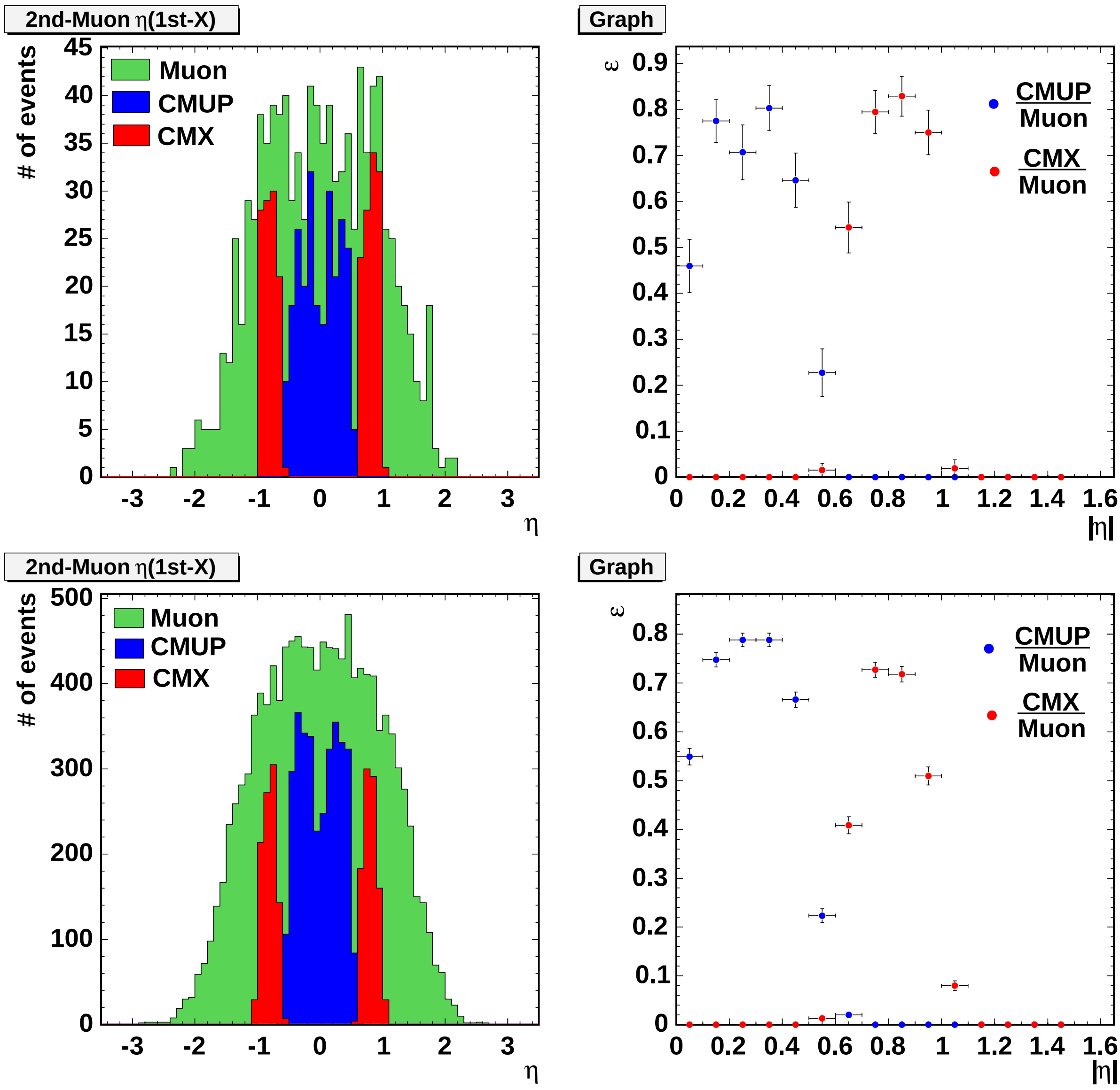

Figure 3.14: The η distribution (left figure) and Reconstrction efficiency each 0.1 η (right one). for the 1st muon CMX. The upper two figures are from Data sample, the lower two figures are MC.

Chapter 4

$\gamma^*/Z^0 \to \ell\ell$ Cross Section

We estimate Cross Section of $\gamma^*/Z^0 \to \ell\ell$ channels due to validate this selection cut efficiencies and Scale Factors. We also compared this cross section with CDF official results [18].

4.1 Total Efficiency

We get the cross section from in the following function

$$\sigma = \frac{N_{\mathrm{obs}}(\mathrm{Data})}{\varepsilon_{\mathrm{tot}}(\mathrm{Data}) \cdot L}, \tag{4.1}$$

where $N_{\mathrm{obs}}(\mathrm{Data})$ is the number of obsereved Z events from Data, $\varepsilon_{\mathrm{tot}}(\mathrm{Data})$ is total efficiency from Data and L is Luminosity of using data. We note that the $\varepsilon_{\mathrm{tot}}(\mathrm{Data})$ is gotten by the following (4.2)

$$\varepsilon_{\mathrm{tot}}(\mathrm{Data}) = \varepsilon_{\mathrm{tot}}(\mathrm{MC}) \cdot \mathrm{SF}^2_{\mathrm{ISO}} \cdot \mathrm{SF}^2_{\mathrm{ID}} \cdot \mathrm{SF}^2_{\mathrm{rec}} \cdot \varepsilon_{\mathrm{trig}}. \tag{4.2}$$

To get the $\varepsilon_{\mathrm{tot}}(\mathrm{MC})$, we count the number of γ^*/Z events, which is HEPG level. Next, we count Z events, which is CDF level. We note that this Z events is exactly Z event, not γ^*/Z^0 event. So, we have to pay attention to γ interfere with Z. Now, we estimate interference factor (f_{inter}, $Z \stackrel{f_{\mathrm{inter}}}{\to} \gamma^*/Z^0$). In HEPG level, we take γ^*/Z^0 mass distribution, and count the number of Z events as same as the lepton selection cut estimation. Moreover, Using a liner function of the fitting funation, count γ^* events, so, we get the interference factor by taking a ratio of the number of γ^* and that of Z,

$$f_{\mathrm{inter}} = \frac{N_{\gamma^*} + N_Z}{N_Z} \tag{4.3}$$

where N_{γ^*} counting is done within $66 < M_{\gamma^*/Z} < 116$ GeV/c^2 due to compare to the CDF Run result. The interference factor is 1.107 for $\gamma^*/Z^0 \to ee$ and 1.111 for $\gamma^*/Z^0 \to \mu\mu$. Figure 4.1 shows γ^*/Z^0 mass distribution in HEPG level. The left figure is $\gamma^*/Z^0 \to ee$, the right one is $\gamma^*/Z^0 \to \mu\mu$. Table 4.1 shows the number of observed γ^*/Z^0 events and the total efficiency for Data and MC.

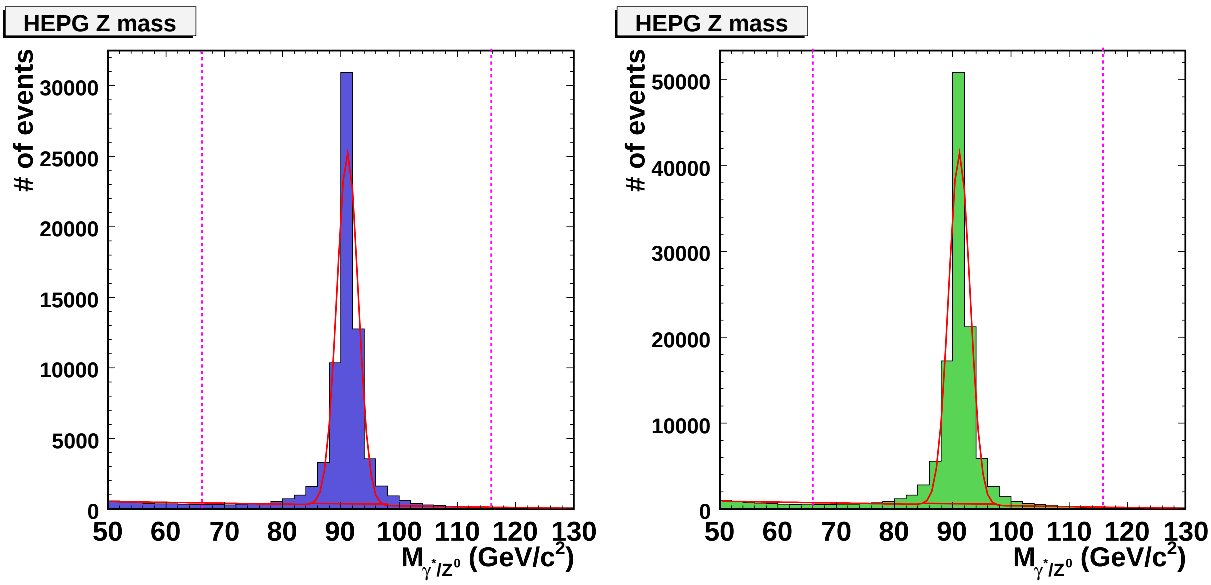

Figure 4.1: γ^*/Z^0 mass distributions in HEPG level. The left figure is $\gamma^*/Z^0 \rightarrow ee$, the right one is $\gamma^*/Z^0 \rightarrow \mu\mu$. The red line is the fitting function.

Type	$N_{\rm obs}$(Data)	$\varepsilon_{\rm tot}$(Data)	$\varepsilon_{\rm tot}$(MC)
CEM-CEM	347	0.0507±0.0018	0.0554±0.0008
CMUP-CMUP	176	0.0141±0.0008	0.0198±0.0003
CMX-CMUP	236	0.0196±0.0014	0.0191±0.0003
CMX-CMX	69	0.0051±0.0004	0.0051±0.0002
CMUP-CMX	236	0.0185±0.0013	0.0191±0.0003

Table 4.1: The number of Observed γ^*/Z^0 events and the Total efficiency for Data and MC.

4.2 Cross Section and Comparing to CDF Run II Result

Using the total efficeincy, Scale Factors and the number of observed γ^*/Z^0 events, we can get γ^*/Z^0 cross section ($66 < M_{\ell\ell} < 116$ GeV/c^2). These cross section is shown in Table 4.2. The left side table shows this corss sections and the CDF Run II official results. We can see that $\gamma^*/Z^0 \rightarrow ee$ cross section is a difference of 9.2% for CDF Run II, while $\gamma^*/Z^0 \rightarrow \mu\mu$ is that of 3.2%. From these differences, We think that this selection cuts is validated for lepton selection. The right side table of Table 4.2 is shown in the cross section breacking down muon types. The CDF result have been estimated for 66 $< M_{\ell\ell} < 116$ GeV/c^2, we also estimated it for same mass region.

Channel	This analysis	CDF Run II	Difference
$\gamma^*/Z^0 \to ee$	232.1±8.1	255.8±3.9	9.2%
$\gamma^*/Z^0 \to \mu\mu$	240.1±8.1	248.0±5.9	3.2%

Muon Type	Cross Section
CMUP-CMUP	238.6±13.3
CMX-CMUP	229.4±15.8
CMX-CMX	260.2±22.6
CMUP-CMX	243.8±16.8

Table 4.2: $\gamma^*/Z^0 \to \ell\ell$ Cross Section (pb) for this analysis and CDF Run II Result (left table, The error is only statistic error). The right side table shows cross section breacking down muon types (CMUP-CMUP, CMX-CMUP, CMX-CMX and CMUP-CMX).

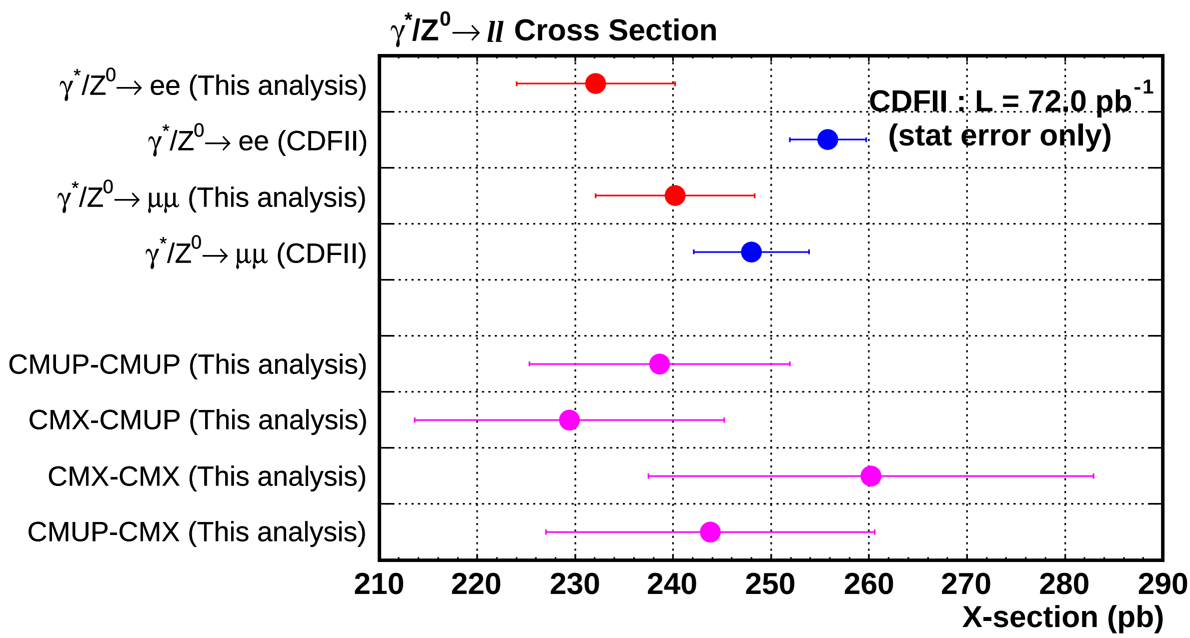

Figure 4.2: $\gamma^*/Z^0 \to \ell\ell$ Cross section for this anlysis and CDF Run II official result.

Chapter 5

Conclusions

We estimated lepton selection cut efficiencies and scale factors. This analysis is for Higgs search in the following mode:

$$qq' \to W^{\pm}H \to W^{\pm}W^{*}W^{*} \to \ell^{\pm}\nu\ell^{\pm}\nu + X.$$

This mode has like-sign dilepton in the final state. So, we have to estimate lepton selection cut efficiency and scale factor. We now used basically standard lepton selection criteria in the CDF analysis. What we should emphasize is that we required kinematical cut of greater than 6 GeV/c^2 to the 2nd leg lepton, while for the 1st leg one, greater than 20 GeV/c^2. At the same time, we compared this efficiency with previous analysis (CDF7262). We also estimated $\gamma^*/Z^0 \to \ell\ell$ cross sections due to validate this selection cut for lepton selection in the CDF Run II data coresponding to an integrated luminosity of 29.4 pb^{-1} for $\gamma^*/Z^0 \to ee$ and that of 52.4 pb^{-1} for $\gamma^*/Z^0 \to \mu\mu$ each. We got the following results:

$$\sigma_{\gamma^*/Z^0 \to ee} = 232.1 \pm 8.1 \text{ pb}$$
$$\sigma_{\gamma^*/Z^0 \to \mu\mu} = 240.1 \pm 8.1 \text{ pb}$$

Therefore more, we compared this cross section with CDF Run II official results. Those comparisons are that for $\gamma^*/Z^0 \to ee$ cross section, the difference of 9.2% and for $\gamma^*/Z^0 \to \mu\mu$, the difference of 3.2% each. From this comparison, we think that this mehods of lepton selection cuts is validated for lepton selection.

Our future plan is that we estimate efficiency for our Higgs event using this lepton selection method, and search for $WH \to WWW$.

Bibliography

[1] Francis Halzen and Alan D. Martin, *"QUARKS & LEPTONS: An Introductory Course in Modern Particle Physics"*, john Wiley & Sons, Inc. (1984).

[2] Donald H. Perkins, *"Introdction to High Energy Physics 4th edition"*, Cambridge University Press (2000).

[3] The LEP Collabrations ALEPH, DELPHI, L3 and OPAL, The LEP Working Group for Higgs Boson Serches, *"Search for the standard Model Higgs Boson at LEP"*, hep-ex/0306033 v1 (2003).

[4] C.W. Smith and C.D. Curtis, *"Operation of the Fermilab H^- Magnetron Source"*, Proc. 4th int. Symp. on the Production of the Fermilab and Neutralization of Negative Ions and Beams, Brookhaven, US, AIP Conf. Proc. No. 158 (1986) 425.

[5] D.E. Young and R.J. Noble, *"400 MeV Upgrade for the Fermilab Linac"*, Fermilab Technical Report, Fermilab-Conf-89/198 (1989).

[6] CDF Collaboration, F. Abe et.al., *"Proposal for Enhancement of the CDF II Datector: An Inner Silicon Layer and A Time of Flight Detector"*, Fermilab-Preposal-909.

[7] CDF Collaboration, T.K. Nelson, *"THe CDF-II silicon tracking system"*, Nul. Instrum. Methods A **360** (1995) 137.

[8] CDF Collaboration, T. Affolder *et al.*, *"CDF Central Outer Tracker"*, Fermilab-Pub-03-355-E (2003), Submitted to Nucl. Instrum. Mathods.

[9] G. Asoli *et al.*, *"CDF Central Muon Detector"*, FERMILAB-PUB-87/181-E, Nucl, Instrum. Mathods A **268** (1988) 33.

[10] L. Balka *et al.*, *"The CDF Central Electromagnatic Calorimater"*, Fermilab-Pub-87-172-E, Nucl. Instrum. Methods, A **267** (1988) 272.

[11] J. Elias *et al.*, *"Luminosity Monitor Based on Cherenkov Counters for $p\bar{p}$ Colliders"*, Fermilab-Pub-99/191, Nucl. Inatrum. Methods. A **441** (2000) 366.

[12] Mireca Coca, Eva Halkiadakis, Sarah Lockwitz, *"Central Electron Identification Efficiencies for Summer 2003 conferences"*, CDF note 6580 v1.0 (2003).

[13] Victoria Martin, *"High-p_T Muon ID Cuts and Efficiencies for use with* `5.3.1` *Data and* `5.3.3` *MC"*, CDF note 7367 (2005).

[14] Jason Nielsen, Lauren Tompkins, Doug Hoffman, Young-Kee Kim and Greg Veramendi *"Trigger Efficiencies for High E_T Electrons"* CDF note 6234 (2004).

[15] Victoria Martin, *"High-p_T muons, reconmmened cuts and efficiencies for release* `5.3`*"*, CDF note 7031 (2004).

[16] Hirokazu Kobayashi, Yoshihiro Seiya and Kazuhiro Yamamoto, *"Search for WH Production Using High-p_T Isolated Like-sign Dilepton Events in Run II"*, CDF note 7262 (2004).

[17] C. Hill, J. Incandela and C. Mills, *"Electron Identification in Offline Release* `5.3`*"*, CDF note 7309 v3.0 (2005).

[18] CDF Collaboration, *"First Measurement of Inclusive W and Z Cross Sections from Run II of Fermilab Tevatron Collider"*, Phys. Rev. Lett. **94**, 091803 (2005).